
Федеральное государственное автономное образовательное учреждение
высшего образования
«Московский физико-технический институт
(национальный исследовательский университет)»
Физтех-школа физики и исследований им. Ландау
Физтех-кластер академической и научной карьеры (Квантовые наноструктуры, материалы и устройства)

Направление подготовки / специальность: 03.04.01 Прикладные математика и физика

Направленность (профиль) подготовки: Общая и прикладная физика

**РЕЗОНАНСНАЯ СПЕКТРОСКОПИЯ ДИНАМИКИ ВИХРЕЙ
СВЕРХПРОВОДЯЩИХ ТОКОВ В ДЖОЗЕФСОНОВСКИХ
ПЛАНАРНЫХ КОНТАКТАХ**

(магистерская диссертация)

Студент:

Калашников Дмитрий Сергеевич

(подпись студента)

Научный руководитель:

Столяров Василий Сергеевич,
канд. физ.-мат. наук

(подпись научного руководителя)

Консультант (при наличии):

(подпись консультанта)

Москва 2022



Skolkovo Institute of Science and Technology

MASTER'S THESIS

**Resonance spectroscopy of the superconducting current
vortices dynamics in planar Josephson junctions**

Master's Educational Program: Photonics and Quantum Materials

Student _____

Dmitrii Kalashnikov
Photonics and Quantum Materials
June 1, 2022

Research Advisor: _____

Anton Andreev
Professor of Physics University of Washington, Seattle, USA

Co-Advisor: _____

Vasily Stolyarov
Director of Centre for Advanced Mesoscience and Nanotechnology (CMN) and
deputy head of Topological Quantum Phenomena in Superconducting Systems
Laboratory (TQPSS), MIPT, Dolgoprudniy, Russia

Moscow 2022

All rights reserved.©

The author hereby grants to Skoltech permission to reproduce and to distribute publicly paper and electronic copies of this thesis document in whole and in part in any medium now known or hereafter created.



Skolkovo Institute of Science and Technology

МАГИСТЕРСКАЯ ДИССЕРТАЦИЯ

**Резонансная спектроскопия динамики вихрей
сверхпроводящих токов в джозефсоновских планарных
контактах**

Магистерская образовательная программа: Фотоника и квантовые материалы

Студент: _____

Калашников Дмитрий Сергеевич
Фотоника и квантовые материалы
Июнь 1, 2022

Научный руководитель: _____

Антонов Андрей Владимирович
Профессор физики Вашингтонского университета, Сиэтл, США

Со-руководитель: _____

Столяров Василий Сергеевич
Исполнительный директор Центра перспективных методов мезофизики и нанотехнологий МФТИ и заместитель заведующего Лаборатории топологических квантовых явлений в сверхпроводящих системах МФТИ, Долгопрудный, Россия

Москва 2022

Все права защищены. ©

Автор настоящим дает Сколковскому институту науки и технологий разрешение на воспроизводство и свободное распространение бумажных и электронных копий настоящей диссертации в целом или частично на любом ныне существующем или созданном в будущем носителе.

Resonance spectroscopy of the superconducting current vortices dynamics in planar Josephson junctions

Dmitrii Kalashnikov

Submitted to the Skolkovo Institute of Science and Technology
on June 1, 2022

Abstract

Currently, new promising concepts of computing systems are being actively developed, which can overcome the existing semiconductor technology in terms of speed and energy efficiency. One of the main directions in this field is superconducting electronics. In this work, a system consisting of a Josephson junction and a coplanar resonator was studied by microwave spectroscopy. Of particular interest was the possibility of using Josephson vortices to change the state of the resonator. The aim of the work was to study the possibility of using this structure as an element of computing systems. Moreover, being a mesoscopic system, Josephson vortices are interesting from a fundamental point of view and new methods of their experimental research can help in the development of this field of science. As a result of the work, states with several Josephson vortices were obtained and investigated, on the basis of which the existence of a surface barrier for vortices is shown. The stability of the system was demonstrated and a method for using Josephson vortices as a memory element in a microwave system was proposed.

Research Advisor:

Name: Anton Andreev

Degree: Professor

Title: Professor of Physics University of Washington, Seattle, USA

Co-Advisor:

Name: Vasily Stolyarov

Degree: PhD

Title: Director of Centre for Advanced Mesoscience and Nanotechnology (CMN) and deputy head of Topological Quantum Phenomena in Superconducting Systems Laboratory (TQPSS), MIPT, Dolgoprudniy, Russia

Резонансная спектроскопия динамики вихрей сверхпроводящих токов в джозефсоновских планарных контактах

Калашников Дмитрий Сергеевич

Представлено в Сколковский институт науки и технологий
Июнь 1, 2022

Реферат

В настоящее время ведется активная разработка новых перспективных концепций вычислительных систем, которые могут превзойти существующую полупроводниковую технологию по быстродействию и энергоэффективности. Одним из основных направлений в этой области является сверхпроводящая электроника. В данной работе исследовалась система из джозефсоновского перехода и копланарного резонатора методом микроволновой спектроскопии. Особый интерес представляла возможность использования Джозефсоновских вихрей для изменения состояния резонатора. Целью работы было исследование возможности использования данной структуры в качестве элемента вычислительных систем. Более того, являясь мезоскопической системой, вихри Джозефсона интересны с фундаментальной точки зрения и новые методы их исследования смогут помочь в развитии этой сферы науки. В результате работы были получены и исследованы состояния с несколькими вихрями Джозефсона, на основе которых показано существование поверхностного барьера для вихрей. Была продемонстрирована стабильность системы и предложен способ использования джозефсоновских вихрей в качестве элемента памяти в СВЧ системе.

Научный руководитель:

Имя: Антонов Андрей Владимирович

Ученое звание, степень: к.ф.-м.н.

Должность: Профессор физики Вашингтонского университета, Сизл, США

Со-руководитель:

Имя: Столяров Василий Сергеевич

Ученое звание, степень: к.ф.-м.н.

Должность: Исполнительный директор Центра перспективных методов мезофизики и нанотехнологий МФТИ и заместитель заведующего Лаборатории топологических квантовых явлений в сверхпроводящих системах МФТИ, Долгопрудный, Россия

Acknowledgments

First of all, I would like to express my great gratitude to my scientific supervisors Anton Andreev and Vasily Stolyarov for the valuable knowledge they gave me, direct assistance in carrying out this work and teaching me the necessary skills for successful experiments. I am grateful to the entire team of the Laboratory of Topological Quantum Phenomena in Superconducting Systems MIPT for their help in mastering experimental equipment and techniques. I would like to express special thanks to the people who have made a significant contribution to this work: Igor Golovchanskiy for his valuable advice, discussion of the results and assistance in the samples fabrication and Andrey Shishkin for assistance in the samples fabrication and training to work in a clean room. I am grateful to the team of the Laboratory of Artificial Quantum Systems MIPT for their help in conducting experiments.

Contents

1	Introduction	9
2	Background	10
2.1	Superconductivity. General information.	10
2.1.1	Main phenomena	10
2.1.2	Ginzburg – Landau theory	10
2.1.3	Type-I and type-II superconductors	11
2.1.4	Abrikosov vortices	12
2.2	Josephson effects	13
2.2.1	Main phenomena	13
2.2.2	The Resistively and Capacitively Shunted Junction Model	14
2.2.3	Josephson junction in the external magnetic field	15
2.2.4	Long Josephson junctions. Josephson vortexes	16
2.3	Microwave engineering	18
2.3.1	Long transmission lines	18
2.3.2	The terminated line	20
2.3.3	S-parameters	21
2.3.4	Resonators from transmission lines	22
3	Technological Methods	25
3.1	Film sputtering	25
3.1.1	General information	25
3.1.2	Used equipment	25
3.2	Lithography	26
3.2.1	General information	26
3.2.2	Used equipment	27
3.3	Etching	30
3.3.1	General information	30
3.3.2	Used equipment	31
4	Experimental Methods	33
4.1	Dilution refrigerator	33
4.1.1	System organization	33
4.1.2	Operating principle	34
4.2	Sample holder	36
4.3	Bonding	37

4.4	Experimental setup	38
5	Samples	40
5.1	Design	40
5.2	Fabrication process	41
5.3	SEM	42
6	Results and Discussion	44
6.1	Resonators spectroscopy	44
6.1.1	Resonators parameters	44
6.1.2	Temperature dependence	45
6.2	Direct current measurements of SNS junctions	46
6.2.1	Current–voltage characteristics	46
6.2.2	Dependence on the magnetic field	48
6.2.3	Dependence on the temperature	48
6.3	Spectroscopy of resonators with SNS	49
6.3.1	Resonances overview	49
6.3.2	RF scan in the magnetic field. Josephson and Abrikosov vortexes detection	50
6.3.3	Analysis of Josephson vortexes	52
6.3.4	Edge barrier effect	53
6.3.5	Switching states	54
6.3.6	Nonlinear response	54
7	Conclusion	56

1 Introduction

Superconducting systems have a number of unique properties due to the quantum nature of the phenomenon. Such systems have been used in various high-precision devices since the middle of the last century, such as picovoltmeters, magnetic field sensors, bolometers, single-photon detectors, THz sources and receivers, and much more [1]. Recently, there has been an active use of Josephson technologies in computing systems. For example, the most famous direction is the development of quantum computers based on superconducting qubits [2]. It should be noting that qubits environment consists of microwave lines and devices and is designed for frequencies of the order of 10 GHz. Another interesting concept of computing systems is Rapid Single Flux Quantum logic, where information is transmitted using magnetic flux quanta in superconducting circuits [3]. Besides, there are attempts to use superconductors in neuromorphic computers [4].

One of the interesting phenomena arising in Josephson junctions is superconducting current vortexes called Josephson vortexes. These structures carry a quantum of magnetic flux. Vortexes are often considered as particles that can interact with each other, with a magnetic field and a flowing current. These objects have long been studied by various methods [5, 6].

In this work, a system consisting of a Josephson SNS junction inserted in a microwave coplanar resonator was studied. The main difference between such a system and direct current measurements is that it is possible to study the effect of vortexes using small microwave currents that do not affect them. Vortexes in the Josephson junction can be controlled using an external magnetic field, while the resonator parameters will change, which can be measured using a microwave signal. In theory, such a system can be used as a logical element and a memory cell. The purpose of this work was to test this hypothesis and experimental implementation of the described system.

2 Background

2.1 Superconductivity. General information.

2.1.1 Main phenomena

Superconductivity is a quantum phenomenon that occurs in some materials at temperatures below the so-called critical temperature (T_c), and is characterized mainly by two effects [7, 8]. The first of them is the absence of electrical resistance. The second effect, discovered by Meissner and Ochsenfeld, is the expulsion of a magnetic field from a superconductor. In other words, a superconductor has the properties of an ideal conductor and a diamagnet. There is a critical magnetic field H_c and a critical current density j_c , exceeding which superconductivity is destroyed. Moreover, the transition to and from a superconducting state with a change in temperature is a phase transition of the II kind, and the transition under the action of a magnetic field is of the I kind.

2.1.2 Ginzburg – Landau theory

To describe the quantum phenomena that appear during the transition of a material to the superconducting state, the Ginzburg – Landau theory was developed, based on the Landau theory of phase transitions of the second kind. As an order parameter, the wave function of superconducting electrons $\Psi(\mathbf{r})$ is used, normalized so that $|\Psi(\mathbf{r})|^2 = n_s(\mathbf{r})/2$, where n_s — density of superconducting electrons. According to the theory of phase transitions of the second kind, the free energy density of a superconductor can be written using the Taylor formula with the small parameter near the critical temperature:

$$f_{s0} = f_n + \alpha|\Psi|^2 + \frac{\beta}{2}|\Psi|^4 \quad (1)$$

where f_n is the free energy density of a superconductor in the normal state.

$$F_{sH} = F_n + \int \left[\alpha|\Psi|^2 + \frac{\beta}{2}|\Psi|^4 + \frac{1}{4m} \left| -i\hbar\nabla\Psi - \frac{2e}{c}\mathbf{A}\Psi \right|^2 + \frac{(\text{rot } \mathbf{A})^2}{8\pi} \right] dV \quad (2)$$

where integration is carried out over the entire volume of the superconductor, \mathbf{A} — vector potential of the magnetic field, F_n — free energy of the superconductor in the normal state.

Minimizing this functional by Ψ^* and \mathbf{A} , the Ginzburg–Landau equations are derived:

$$\alpha\Psi + \beta\Psi|\Psi|^2 + \frac{1}{4m} \left(i\hbar\nabla + \frac{2e}{c}\mathbf{A} \right)^2 \Psi = 0 \quad (3)$$

with a boundary condition

$$\left(i\hbar\nabla\Psi + \frac{2e}{c}\mathbf{A}\Psi \right) \mathbf{n} = 0$$

$$j_s = -\frac{i\hbar e}{2m}(\Psi^*\nabla\Psi - \Psi\nabla\Psi^*) - \frac{2e^2}{mc}|\Psi|^2\mathbf{A} \quad (4)$$

where $j_s = \frac{c}{4\pi} \text{rot rot } \mathbf{A}$ — current density in a superconductor

Define two values of the dimension of length

$$\xi = \sqrt{\frac{\hbar^2}{4m|\alpha|}} \quad (5)$$

$$\lambda_L = \sqrt{\frac{mc^2\beta}{8\pi e^2|\alpha|}} = \sqrt{\frac{mc^2}{4\pi n_{s0}e^2}} \quad (6)$$

The parameter ξ introduced in the Ginzburg–Landau theory is called the coherence length, the physical meaning of which is the characteristic distance at which the wave function ψ changes. The parameter λ_L is called the penetration depth of the magnetic field. The dimensionless value $\kappa = \lambda/\xi$ is called the Ginzburg–Landau parameter.

2.1.3 Type-I and type-II superconductors

The division of superconductors into the type-I and type-II groups was proposed by A. A. Abrikosov, who theoretically described the distinctive properties of type-II superconductors. Two critical fields are defined for them: B_{c1} and B_{c2} . At fields $B < B_{c1}$, a type II superconductor is an absolute diamagnet, when the field increases $B_{c1} < B < B_{c2}$, the superconductor changes to a so-called mixed state in which the magnetic field begins to partially penetrate the sample, in large fields $B > B_{c2}$ superconductivity is destroyed and the material goes into a normal state. In the mixed state, the magnetic field penetrates the superconductor in the form of separate threads, which are cylinders elongated along the direction of the external field, which have a normal core of the radius of the order of the coherence length ξ . A superconducting current called the Abrikosov vortex flows around this core. The magnetic field flux enclosed in one vortex is equal to $\Phi_0 = \frac{h}{2e}$. The existence of a mixed state is connected with the surface energy at the boundary between the superconducting and normal states σ_{ns} , which depends on the parameters λ and ξ . If $\kappa < 1/\sqrt{2}$, then $\sigma_{ns} > 0$ and the sample is a superconductor of the type-I,

if $\kappa > 1/\sqrt{2}$, then $\sigma_{ns} < 0$ and the sample is a type-II superconductor. The relation of critical fields with λ and ξ for the case of $\kappa \gg 1$ is determined by the formulas:

$$B_{c1} = \frac{\Phi_0}{4\pi\lambda^2} (\ln \kappa + 0.50) \quad (7a)$$

$$B_{c2} = \frac{\Phi_0}{2\pi\xi^2} \quad (7b)$$

2.1.4 Abrikosov vortices

According to the Ginzburg – Landau equations we can write the magnetic field distribution of a single Abrikosov vortex for $r \gg \xi$, under of the assumption $\kappa \gg 1$:

$$H(r) = \frac{\Phi_0}{2\pi\lambda^2} K_0(r/\lambda) \quad (8)$$

,where $K_0(x)$ is Macdonald function, which asymptotic behavior is:

$$K_0(z) \propto \begin{cases} \ln z, & z \ll 1, \\ e^{-z}/\sqrt{z}, & z \gg 1. \end{cases} \quad (9)$$

A graphical representation of the distribution of the magnetic field of the vortex and the order parameter is shown in Fig. 1.

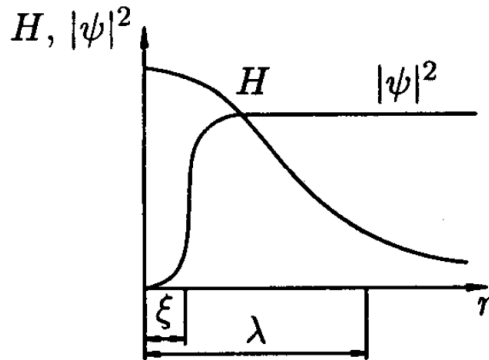


Figure 1: Distribution of the order parameter and the magnetic field created by the Abrikosov vortex.

2.2 Josephson effects

2.2.1 Main phenomena

In 1962, Brian Josephson in his work [9], considering the tunnel contact of two superconductors, showed two important effects that occur in this system. The first, or stationary Josephson effect, is the possibility of a superconducting tunneling current flowing through the junction if the magnitude of this current is less than a certain critical value. The second, or non-stationary Josephson effect, is the emission of electromagnetic radiation if the current flowing through the junction exceeds a critical value.

Nowadays, it is now known that the Josephson effects occur not only in tunnel contacts, but also in any junction with a region where superconductivity is absent or strongly suppressed [1]. Among others, there are contacts with such materials as: insulator (SIS), normal metal (SNS), ferromagnet (SFS), a narrow section of a superconductor (Dayem bridge).

Mathematically, the Josephson effects are described in terms of the phase difference of the superconducting wave function between the contact electrodes φ [10]. For a tunnel contact, the relationship between the superconducting current and the phase difference is:

$$I_s(\varphi) = I_c \sin \varphi \quad (10)$$

This is the first Josephson equation or current-phase relation for the case of a tunnel contact. In general, the current-phase ratio must satisfy only the symmetry conditions and can be written as a Fourier series:

$$I_s(\varphi) = I_c \sin \varphi + \sum_{n=2}^{\infty} I_n \sin n\varphi \quad (11)$$

The non-stationary Josephson effect is described by the phase change over time and connected with the appearance of the voltage at the contact:

$$\hbar \frac{\partial \varphi}{\partial t} = 2eV \quad (12)$$

2.2.2 The Resistively and Capacitively Shunted Junction Model

When considering the Josephson contact as an element of an electrical circuit, the resistively and capacitively shunted model is used. In this model, the current through the junction can flow through several parallel channels: superconducting current (for which the expression (11) is valid), normal current (for which Ohm's law is valid), and the last one, for tunnel contacts, displacement current. Based on this model, the Josephson junction can be represented as a superconducting junction, a resistor (R_N) and a capacitor (C) connected in parallel (see Fig.). For contacts with a conductive layer $C = 0$. In such a system, the total current will be equal to:

$$I = I_s(\varphi) + \frac{V}{R_N} + C \frac{dV}{dt} \quad (13)$$

Using the second Josephson equation (12), we can obtain a differential equation for the phase difference in the junction:

$$I = I_s(\varphi) + \frac{1}{R_N} \frac{\Phi_0}{2\pi} \frac{d\varphi}{dt} + C \frac{\Phi_0}{2\pi} \frac{d^2\varphi}{dt^2} \quad (14)$$

Since this is a second-order nonlinear differential equation, there is no general analytical solution. However, there are conditions under which the equation (14) is solved analytically: suppose that $I_s(\varphi) = I_c \sin \varphi$ and $C = 0$, then:

$$I = I_c \sin \varphi + \frac{1}{R_N} \frac{\Phi_0}{2\pi} \frac{d\varphi}{dt} \quad (15)$$

The voltage at the junction at $I > I_c$ is determined by the formula:

$$V(t) = R_N \frac{I^2 - I_c^2}{I + I_c \cos \omega t}, \quad \text{where} \quad (16a)$$

$$\omega(t) = \frac{2\pi}{\Phi_0} R_N \sqrt{I^2 - I_c^2} \quad (16b)$$

However, it should be noted that standard voltmeters accumulate and average data over a sufficiently long period of time, so the measured value will be equal to the average voltage over the period:

$$\langle V \rangle = R_N \sqrt{I^2 - I_c^2} \quad (17)$$

Current–voltage characteristic for the case of an SNS contact is shown in Fig. 2 For the case of tunnel contact, in general, the capacity value in the expression (14) cannot be

neglected, then this equation can be solved numerically. The qualitative difference of the case with $C \neq 0$ is the presence of inertia in the system, because of this, hysteresis is observed on the current–voltage characteristic of the SIS contact (see Fig. 2).

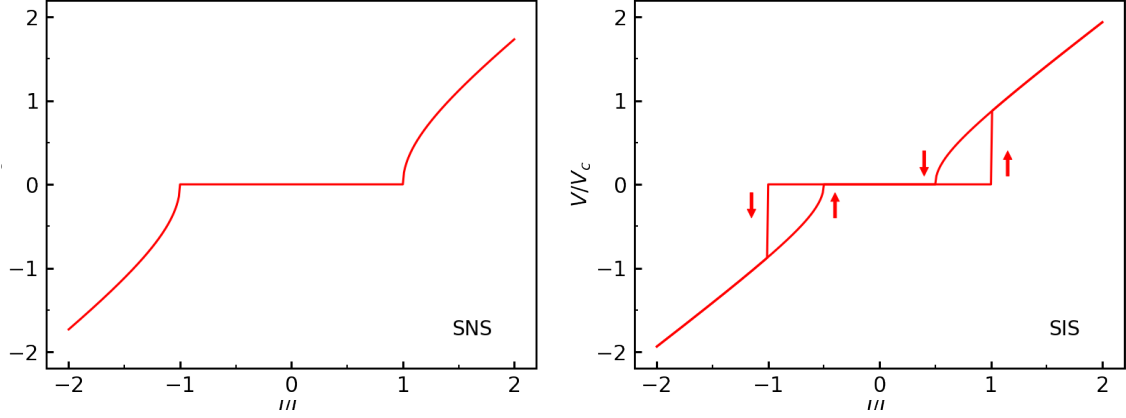


Figure 2: Current–voltage characteristics of Josephson junctions of SNS (left) and SIS (right) types

2.2.3 Josephson junction in the external magnetic field

The effects of interference of the superconducting wave function are very pronounced in Josephson junctions. The phase of the wave function depends on the magnetic field:

$$\frac{\partial\varphi}{\partial x} = \frac{2\pi}{\Phi_0} t_B B_y \quad (18)$$

Due to the phase change, the maximal superconducting current that can flow through the junction also changes. In the simplest case, when the magnetic field is uniform inside the contact and is equal to the external magnetic field, the expression for this current is:

$$I_{\max} = I_c \left| \frac{\sin(\pi\Phi/\Phi_0)}{(\pi\Phi/\Phi_0)} \right| \quad (19)$$

This expression is exactly equal to the spatial distribution of the average amplitude of the electric field in an optical experiment with a single slit in the Fraunhofer limit.

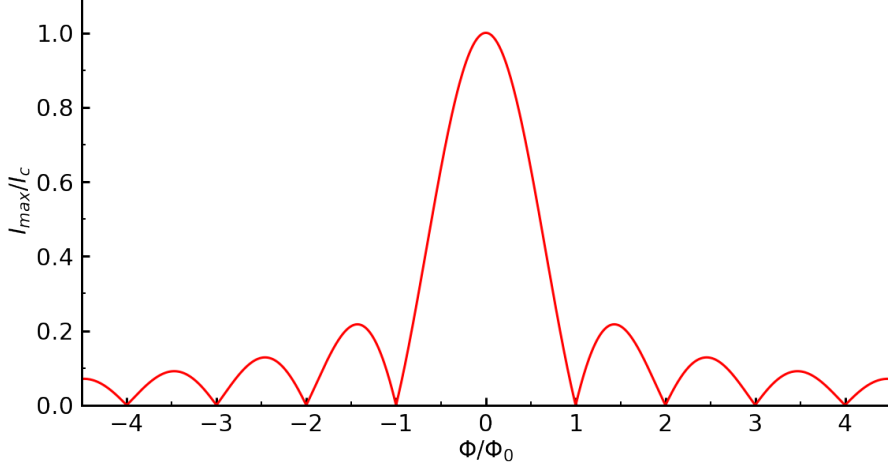


Figure 3: Dependence of the maximum superconducting current through the Josephson junction on the external magnetic field for the case of a short contact

2.2.4 Long Josephson junctions. Josephson vortices

The Fraunhofer dependence of the maximum superconducting current on the magnetic field is valid only for narrow Josephson junctions where the internal magnetic field is homogeneous. As the contact width increases, the magnetic field begins to be shielded by superconducting currents. Firstly consider a stationary problem in which there is no voltage at the junction. To take into account the influence of currents on the magnetic field, use Maxwell's equation:

$$\frac{\partial B_y}{\partial x} = \mu_0 j_z \quad (20)$$

Since there is no voltage at the junction in the considered case, the entire current is superconducting, i.e. $j_z = j_s$, where $j_s = j_c \sin \varphi$ according to the first Josephson equation (11). Substituting the relation of the phase difference and the magnetic field (18) into the expression above, we obtain the ratio:

$$\frac{\partial^2 \varphi}{\partial x^2} = \frac{1}{\lambda_J^2} \sin \varphi \quad (21)$$

,where

$$\lambda_J = \sqrt{\frac{\Phi_0}{2\pi\mu_0 t_B j_c}} \quad (22)$$

This parameter is called the Josephson length and has the meaning of the penetration

depth of a small magnetic field into a long Josephson junction. One of the solutions of the equation (21) has the form:

$$\varphi(x) = 4 \arctan \exp(x/\lambda_J) \quad (23a)$$

$$B(x) = \frac{\Phi_0}{\pi t_B \lambda_J} \frac{1}{\cosh(x/\lambda_J)} \quad (23b)$$

$$j(x) = 2j_c \frac{\sinh(x/\lambda_J)}{\cosh^2(x/\lambda_J)} \quad (23c)$$

This solution is a stationary localized vortex of superconducting current, which is called the Josephson vortex. The graphs of the functions above are plotted on the Fig. 4.

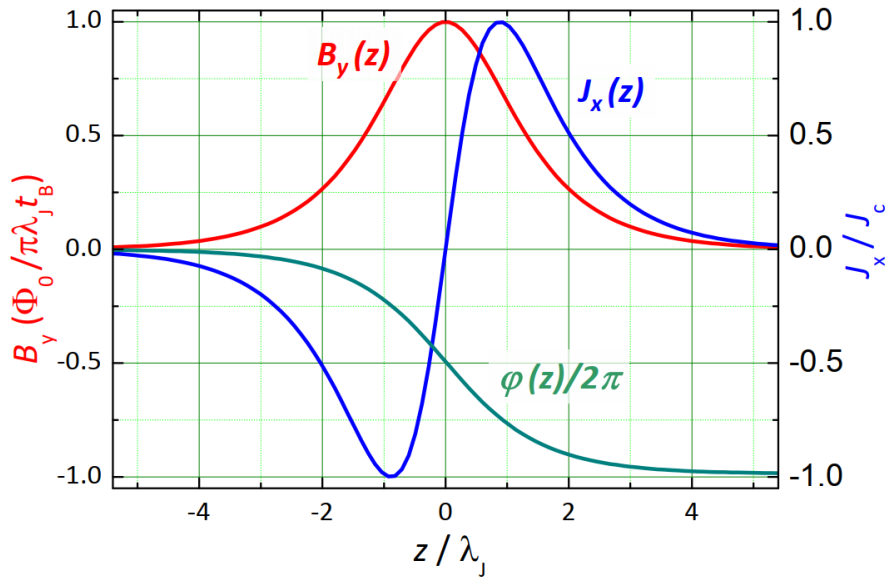


Figure 4: Spatial distribution of the phase difference, magnetic field and current density of the single Josephson vortex in the infinite width junction [10].

In non-stationary case, an electric field appears in the junction according to the second Josephson equation (12):

$$\frac{\partial \varphi}{\partial t} = \frac{2\pi}{\Phi_0} dE_z \quad (24)$$

The electric field will be added to Maxwell's equation and to the expression for the current density:

$$\frac{\partial B_y}{\partial x} = \mu_0 j_z + \varepsilon \varepsilon_0 \mu_0 \frac{\partial E_z}{\partial t}, \quad \text{where} \quad (25a)$$

$$j_z = j_c \sin \varphi + \sigma_N E_z \quad (25b)$$

As a result, we obtain the sine-Gordon equation with the dissipative part, which describes the dynamics of Josephson vortices:

$$\frac{1}{c^2} \frac{\partial^2 \varphi}{\partial t^2} + \frac{\beta}{c^2} \frac{\partial \varphi}{\partial t} - \frac{\partial^2 \varphi}{\partial x^2} + \frac{1}{\lambda_J^2} \sin \varphi = 0 \quad (26)$$

, where $\beta = \sigma_N / (\varepsilon \varepsilon_0)$.

2.3 Microwave engineering

2.3.1 Long transmission lines

Long transmission lines are called electric circuits, the length of which is commensurate with the wavelength of the radiation propagating through it. In this case, the current and voltage in the circuit cannot be considered quasi-stationary, but it is necessary to consider their dependence on the coordinate along the wire. Consider the simplest scheme of a long transmission line consisting of two conductors. To derive the equations, consider a section of a line of small length Δz , as shown in Fig. 5, and enter the following system characteristics per unit length [11]:

R - series resistance per unit length, for both conductors

L - series inductance per unit length, for both conductors

G - shunt conductance per unit length

C - shunt capacitance per unit length

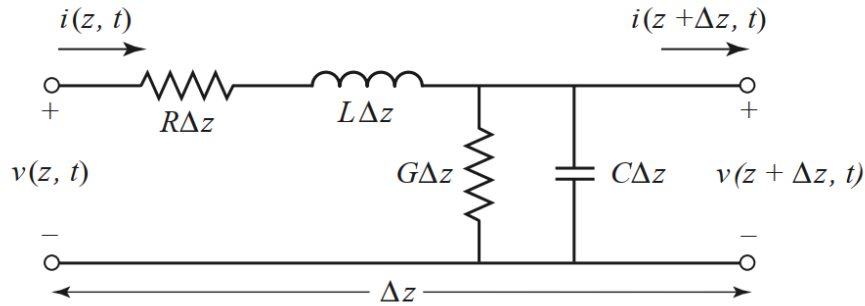


Figure 5: Equivalent scheme for a long transmission line [11].

Using the Kirchhoff's equations for the equivalent long transmission line scheme and going to the limit of $\Delta z \rightarrow 0$, the basic equations known as telegraphic equations are derived:

$$\frac{\partial V(z,t)}{\partial z} = -RI(z,t) - L \frac{\partial I(z,t)}{\partial t} \quad (27a)$$

$$\frac{\partial I(z,t)}{\partial z} = -GV(z,t) - C \frac{\partial V(z,t)}{\partial t} \quad (27b)$$

The solutions of these equations are traveling damped waves:

$$V(z,t) = V_0^+ e^{-\gamma z + i\omega t} + V_0^- e^{\gamma z + i\omega t} \quad (28a)$$

$$I(z,t) = I_0^+ e^{-\gamma z + i\omega t} + I_0^- e^{\gamma z + i\omega t} \quad (28b)$$

, where

$$\gamma = \alpha + i\beta = \sqrt{(R + i\omega L)(G + i\omega C)} \quad (29)$$

The attenuation of the waves depends on the real part of γ . The oscillations, in turn, are described by the imaginary part of γ , for example, the phase velocity of wave propagation is:

$$v_p = \frac{\omega}{\beta} \quad (30)$$

An important characteristic of electrical circuits is their impedance Z_0 , which is equal to:

$$Z_0 = \frac{V_0^+}{I_0^+} = \sqrt{\frac{R + i\omega L}{G + i\omega C}} \quad (31)$$

The lossless line is an important special case of transmission lines when $R = G = 0$. In that case:

$$\gamma = i\omega\sqrt{LC} \quad (32)$$

Then solutions of the telegraphic equations (28a), (28b) of traveling waves. The phase velocity of such waves is equal to:

$$v_p = \frac{1}{\sqrt{LC}} \quad (33)$$

And the expression for the impedance of the system is greatly simplified and no longer depends on the frequency:

$$Z_0 = \sqrt{\frac{L}{C}} \quad (34)$$

The **low-loss line** is described taking into account the nonzero, small values of $R \ll \omega L$, $G \ll \omega C$. In this case, the wave attenuation parameter in the first approximation will be written as:

$$\alpha \approx \frac{1}{2} \left(R\sqrt{\frac{C}{L}} + G\sqrt{\frac{L}{C}} \right) \quad (35)$$

2.3.2 The terminated line

Figure 6 shows a section of a transmission line, which at the point $z = 0$ is terminated in a load impedance Z_L .

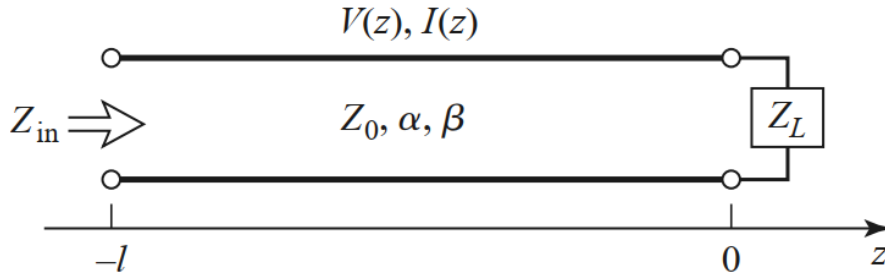


Figure 6: A transmission line terminated in the impedance Z_L [11].

According to the general solutions of the telegraph equations (28a) and (28b) and the ratio between the amplitudes, which is determined by the value Z_0 , the voltage and current distributions are a superposition of two waves propagating to the right and left. The impedance Z_L is essentially a boundary condition and determines the ratio between current and voltage at the point $z = 0$:

$$Z_L = \frac{V(0)}{I(0)} \quad (36)$$

Introduce an important characteristic of a loaded long line – the voltage reflection coefficient:

$$\Gamma = \frac{V_0^-}{V_0^+} = \frac{Z_L - Z_0}{Z_L + Z_0} \quad (37)$$

Using this value, it is possible to transform the general solutions of the telegraph equations (28a) and (28b) for a terminated line (the scheme is shown in Fig. 6):

$$V(z) = V_0^+ (e^{-\gamma z} + \Gamma e^{\gamma z}) \quad (38a)$$

$$I(z) = \frac{V_0^+}{Z_0} (e^{-\gamma z} - \Gamma e^{\gamma z}) \quad (38b)$$

These expressions, up to a common multiplier, determine the distribution of voltage and current in a terminated line. The useful value is the so-called input impedance of the line Z_{in} :

$$Z_{in} = \frac{V(-l)}{I(-l)} = Z_0 \frac{Z_L + Z_0 \tanh \gamma l}{Z_0 + Z_L \tanh \gamma l} \quad (39)$$

It is possible to calculate the power that is delivered to the section of the loaded line at the point $z = -l$:

$$P_{in} = \frac{1}{2} \text{Re}\{V(-l)I^*(-l)\} = \frac{|V_0^+|^2}{2Z_0} (e^{2\alpha l} - |\Gamma|^2 e^{-2\alpha l}) \quad (40)$$

and the power that is delivered to the load at the point $z = 0$:

$$P_L = \frac{1}{2} \text{Re}\{V(0)I^*(0)\} = \frac{|V_0^+|^2}{2Z_0} (1 - |\Gamma|^2) \quad (41)$$

The difference of these powers determines the power of losses on this section of the line:

$$P_{loss} = P_{in} - P_L = \frac{|V_0^+|^2}{2Z_0} [(e^{2\alpha l} - 1) + |\Gamma|^2 (1 - e^{-2\alpha l})] \quad (42)$$

2.3.3 S-parameters

For analysis of microwave devices with one or more transmission lines connected, it is convenient to use the so-called S-parameters, which are elements of the scattering matrix. Let the device have N ports, the amplitude of the wave incident on the port n is equal to V_n^+ , and the amplitude of the reflected wave is equal to V_n^- . The scattering matrix determines the relationship between these values according to the following formula:

$$\begin{pmatrix} V_1^- \\ V_2^- \\ \vdots \\ V_N^- \end{pmatrix} = \begin{pmatrix} S_{11} & S_{12} & \dots & S_{1N} \\ S_{21} & S_{22} & \dots & S_{2N} \\ & & \dots & \\ S_{N1} & & \dots & S_{NN} \end{pmatrix} \begin{pmatrix} V_1^+ \\ V_2^+ \\ \vdots \\ V_N^+ \end{pmatrix} \quad (43)$$

A common situation is when the device has two ports. In that case

$$\begin{pmatrix} V_1^- \\ V_2^- \end{pmatrix} = \begin{pmatrix} S_{11} & S_{12} \\ S_{21} & S_{22} \end{pmatrix} \begin{pmatrix} V_1^+ \\ V_2^+ \end{pmatrix} \quad (44)$$

Consider a situation when a wave from a generator with an amplitude of V_1^+ falls on the input port (port 1), and a wave from a device with an amplitude of V_2^- propagates from the output port (port 2). In addition, the system has a wave reflected from port 1 with an amplitude of V_1^- , but $V_2^+ = 0$, since there is no incident wave on port 2. Then the values are uniquely determined:

$$S_{11} = \frac{V_1^-}{V_1^+} \quad (45a)$$

$$S_{21} = \frac{V_2^-}{V_1^+} \quad (45b)$$

2.3.4 Resonators from transmission lines

A long transmission line can be a base for some RF devices. An example of such devices are resonators, which just are sections of a transmission line with different boundary conditions: at the ends, the line can either be closed ($Z_L = 0$) or open ($Z_L = \infty$). Depending on the combination of these conditions at the two boundaries, the resonators are divided into:

- open $\lambda/2$ resonator: $Z_{L1} = Z_{L2} = \infty$
- closed $\lambda/2$ resonator: $Z_{L1} = Z_{L2} = 0$
- $\lambda/4$ resonator: $Z_{L1} = \infty, Z_{L2} = 0$

The resonator $\lambda/4$ is a section of a transmission line of some length l , shorted on one side (at the point $z = 0$) and open on the other (at the point $z = -l$). Everywhere else, the impedance of the resonator line will be denoted by Z_{0r} . Practical application is mainly found in resonators with high quality factor. Which means low power losses in the line, therefore the parameters for the low-loss transmission line can be used in the analysis. The input impedance of the resonator according to the formula (39) is equal to:

$$Z_{\lambda/4} = Z_{0r} \tanh(\alpha + i\beta)l = Z_{0r} \frac{1 - i \tanh \alpha l \cot \beta l}{\tanh \alpha l - i \cot \beta l} \quad (46)$$

This impedance as a function of frequency has a resonant peak at the frequency:

$$f_{\lambda/4}^{(n)} = \frac{2n-1}{4l\sqrt{LC}}, \quad n \in \mathbb{N} \quad (47)$$

At this frequency $\beta_n l = \frac{\pi}{2}(2n-1)$ or $l = \frac{\lambda}{4}(2n-1)$. With $n=1$ obtain $l = \lambda/4$, so the resonator is called $\lambda/4$. Assuming the losses are small $\alpha l \ll 1$ and considering the small neighborhood of the resonant frequency $\Delta f = f - f_{\lambda/4}^{(n)}$, where $|\Delta f| \ll f_1$, we can simplify the expression for the resonator impedance:

$$Z_{\lambda/4} \simeq \frac{Z_{0r}}{\alpha l + i\frac{\pi}{2}\Delta f/f_1} \quad (48)$$

Quality factor is an important characteristic of the resonator. In this case, the internal Q-factor of the resonator is determined as:

$$Q_i = \omega_r \frac{\langle W_\Sigma \rangle}{P_{loss}} \quad (49)$$

where ω_r is the resonant frequency, $\langle W_\Sigma \rangle = \langle W_e \rangle + \langle W_m \rangle$ — the average energy in the resonator, that is equal to the sum of the average electric and magnetic energies in the resonator, respectively, P_{loss} — loss power.

In the $\lambda/4$ resonator, the internal Q-factor turns out to be equal to:

$$Q_i = \frac{\pi}{4\alpha l}(2n-1) \quad (50)$$

S-parameters of the resonator $\lambda/4$. In the experiment, the S-parameters of the coupled resonator can be measured. We assume that the impedance of the supply line coincides with the impedance of the resonator line, which is equal to Z_0 , then

$$S_{21} = 1 - \frac{Q_l/Q_c}{1 + 2iQ_l(f/f_r^{(n)} - 1)} \quad (51)$$

Resonator with a load. If the resonator $\lambda/4$ in the place of the connection of the central line with the ground is terminated in a small impedance $Z_L = Z_{0r}(r_L + ix_L)$, $r_L \ll 1$ and $x_L \ll 1$, then its characteristics will change as follows:

$$\tilde{f}_r^{(n)} = f_r^{(n)} \left(1 - \frac{2}{\pi(2n-1)} \frac{x_L}{Z_0} \right) \quad (52)$$

$$\frac{1}{\widetilde{Q}_i} = \frac{1}{Q_i} + \frac{4}{\pi(2n-1)} r_L \quad (53)$$

3 Technological Methods

3.1 Film sputtering

3.1.1 General information

Film sputtering includes three main processes: spraying of atoms (molecules) of the source of the desired material, their transfer to the substrate on which this material should be deposited, and the actual deposition process.

3.1.2 Used equipment



Figure 7: Left — electron beam sputtering system Plassys MEB 550 S. Right — custom developed magnetron sputtering setup

Magnetron sputtering In this work, a copper/niobium bilayer was deposited onto empty substrates using a custom developed magnetron sputtering setup. The substrates were previously washed in acetone and IPA, and also cleaned by physical etching in argon plasma inside the spraying unit directly before film sputtering.

Table 1: Copper/niobium magnetron sputtering recipe

Surface cleaning	Duration	20 s, 3 times with 30 s pauses
	Ar pressure	2.1E-2 mbar
	AC power	80 W
	Bias voltage	590 V
Cu sputtering	Residual pressure	1.44E-6 mbar
	Ar pressure	4.0E-3 mbar
	AC power	200 W
	Bias voltage	483 V
Nb sputtering	Residual pressure	1.15E-6 mbar
	Ar pressure	4.0E-3 mbar
	AC power	200 W
	Bias voltage	463 V

Electron beam sputtering In this work, aluminum masks were applied by electron beam sputtering for subsequent etching of gaps for SNS contacts. For this purpose, the Plassys MEB 550 S system was used in the MIPT Collective Use Center.

Table 2: Aluminum electron beam sputtering and removal recipe

Al sputtering	Residual pressure	7.0E-7 mbar
	Emission current	170 mA
	Sputtering rate	0.07 nm/s
Al removal	Solution	KOH 1%, 15 s

3.2 Lithography

3.2.1 General information

Lithography is one of the main processes in the fabrication of nanostructures [12]. Lithography is based on the use of substances, resists, whose properties, mainly solubility, change under high energy radiation. The main stages of lithography are:

- coating a sample with a resist
- irradiation (exposure)
- developing - dissolving only the target area of the resist
- sputtering the material or etching
- dissolving the remaining resist

Resists are most often organic multicomponent polymer compositions that are sensitive to the effects of some high-energy radiation. According to the reaction to radiation, resists are divided into positive (when the illuminated area becomes more soluble and goes away during development) and negative (when the illuminated area becomes less soluble and remains during development).

The following types of lithography by the method of exposure are the most common:

1) Optical mask lithography. For exposure, light in the visible or ultraviolet range is used, which exposure a resist through a previously manufactured mask. This type of lithography is widely used in the industrial production of nanostructures, where it is necessary to create many samples with the same template.

2) Optical laser lithography. The exposure of the resist occurs by focused laser radiation. The laser beam moves and sequentially illuminates the surface areas according to the path loaded into the lithograph. Unlike mask lithography, when using a scanning laser, there is no need for pre-made physical masks, that makes this type of lithography more flexible and convenient at the research and development stage.

3) Electron beam lithography. The resist is exposed by a focused electron beam. This beam is focused and moved with high precision using a system of magnetic lenses. The electron beam, as in the case of laser lithography, consistently illuminates areas of the surface according to the path loaded into the lithograph. The main advantage of EBL is high resolution, so this method is widely used when creating structures in the range from 500 to 20 nm. The main disadvantage is the low speed of exposure.

3.2.2 Used equipment

At different stages of sample fabrication, two types of lithography were used: optical laser lithography — to create large structures such as waveguides and resonators, and electron beam lithography — to create Josephson junctions.

Laser lithography The fabrication of large structures was carried out in a clean room of the Laboratory of Superconducting Metamaterials in MISIS. The laser lithograph Heidelberg uPG 501 and positive photoresist S1813 G2 were used for lithography.

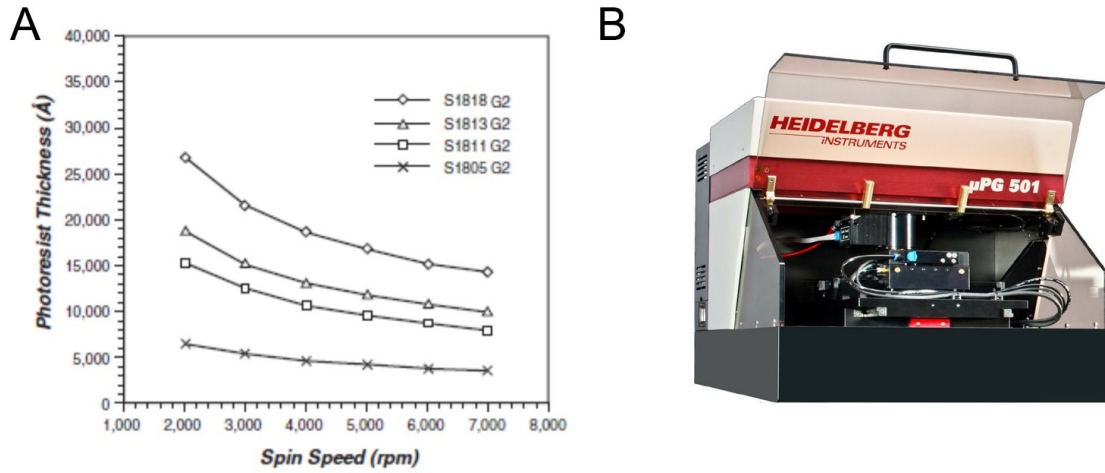


Figure 8: A — the dependence of the thickness of optical resists of the S18xx G2 series after spin coating on the rotation speed. B — laser lithograph Heidelberg uPG 501

Table 3: Laser lithography recipe

Sample preparing	Cleaning	Acetone, ultrasound 1 min
	Pre-baking	—
Resist	Name	S1813 G2
	Spinning	4000 rpm, 60 s
	Baking	hot plate 125 °C, 50 s
	Developing	KOH 8%, 60 s
	Solving	Acetone 60 s, ultrasound 30 s
Lithograph	Dose	85 μC

Electron beam lithography To create the Josephson junctions, it is necessary to etch a gap with a width of 200–300 nm. To do this, an electron beam lithograph Crystal CABLE-9000C in the MIPT Collective Use Center and a positive electron resist PMMA A4 950K were used.

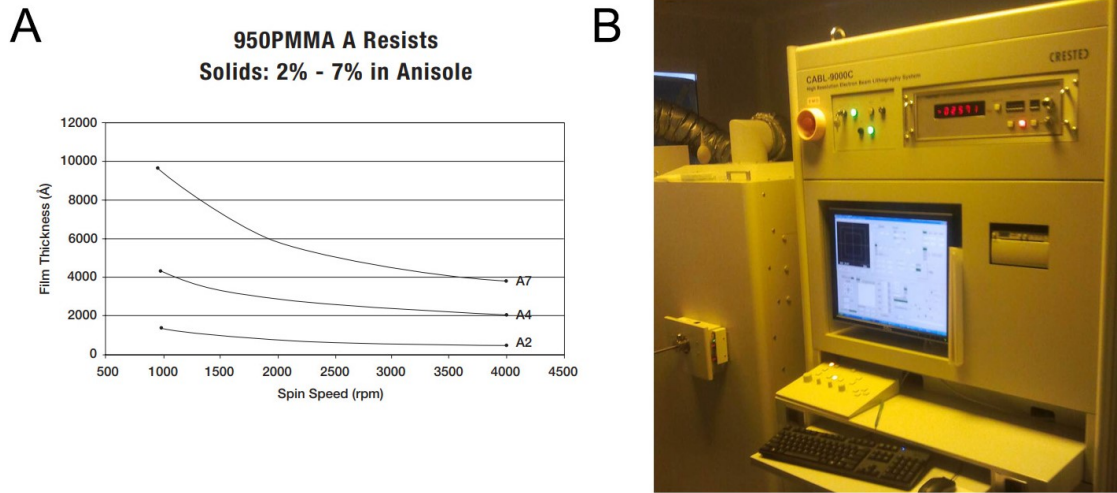


Figure 9: A — the dependence of the thickness of electron resists of the PMMA Ax series after spin coating on the rotation speed. B — electron lithograph Crestec CABL-9000C

Table 4: EBL recipe for aluminium mask fabrication

Sample preparing	Cleaning	Acetone, IPA
	Pre-baking	hotplate 160 °C, 10 min
Resist	Name	AR-P 6200.04
	Spinning	4000 rpm, 1 min
	Baking	hotplate 150 °C, 5 min
	Developing	1) AR600-546, 60 s 2) IPA, 30 s
	Solving	lift-off NMP, 12 hours; 80 °C, 5 min
Lithograph	Current	220 pA
	Time in a point	1 μ s
	Dose	130 μ C/cm ²
	Field	300 \times 300 μ m ²
	Number of points	20000

Table 5: EBL recipe for the protecting layer

Sample preparing	Cleaning	Acetone, IPA
	Pre-baking	hotplate 160 °C, 10 min
Resist	Name	PMMA A4 950K
	Spinning	4000 rpm, 1 min
	Baking	hotplate 160 °C, 5 min
	Developing	1) MIBK + IPA (1:3), 90 s; 2) IPA, 30 s
	Solving	NMP, 80 °C, 5 min
Lithograph	Current	1.1 nA
	Time in a point	1 μ s
	Dose	500 μ C/cm ²
	Field	300 \times 300 μ m ²
	Number of points	20000

3.3 Etching

3.3.1 General information

Etching is the process of selectively removing material from a sample through a pre-prepared mask. There is a wide variety of etching methods. They are divided into two main categories: wet and dry etching.

In dry etching, materials are etched in the gas or vapor phase without wet chemicals. It is also common to differentiate between: physical sputter/ion etching and ion-beam etching (IBE), chemical plasma etching (PE), and synergetic reactive ion etching (RIE):

- in physical sputter/ion etching (IBE), etching occurs as a consequence of a purely physical effect, namely, momentum transfer between energetic Ar⁺ ions and the substrate surface;
- in chemical plasma etching (PE), neutral chemical species such as chlorine or fluorine atoms generated in the plasma diffuse to the substrate, where they react to form volatile products with the layer to be removed. The only role of the plasma is to supply gaseous, reactive etchant species;
- in the case of physical/chemical etching or reactive ion etching (RIE), line-of-sight-impacting ions damage the surface, inducing highly anisotropic chemical reactions

of the surface with plasma neutrals, or, alternatively, a passivating layer is cleared by the ion bombardment, clearing horizontal surfaces only and again resulting in highly anisotropic etching.

3.3.2 Used equipment

Dry plasma chemical etching In this work, niobium was removed by plasma chemical etching process using Sentech setup in MISIS.

Table 6: The recipe for the niobium plasma chemical etching

Plasma	CF ₄ + O ₂
CF ₄ flow	40 sccm
O ₂	5 sccm
Pressure	9 Pa
RF power	90 W
Etching speed	2.4 nm/s

Dry plasma physical etching In this work, small areas of copper was additionally removed by plasma physical etching process using Corial setup in the MIPT Collective Use Center.

Table 7: The recipe for the copper plasma physical etching

Plasma	Ar
Ar flow	30 sccm
Pressure	2.6 mTorr
RF power	50 W
Etching speed	60 nm / min

Wet etching To create resonators and structures for DC measurements in this work, the copper layer was removed using liquid chemical etching process in a clean room of the laboratory in MISIS.

Table 8: The recipe for the copper wet chemical etching

Solution	$[(\text{FeCl}_3:\text{H}_2\text{O})1:3]:\text{H}_2\text{O}$ 1:120
Etching speed	40—50 nm/min

4 Experimental Methods

4.1 Dilution refrigerator

4.1.1 System organization

The refrigerator consists of six metal plates (flanges) located one above the other, which are separated from each other by heat-switchers (see Fig. 10, [13]). These flanges are surrounded by four shells of screens that protect them from heat transfer through radiation (not shown in the picture). The external screen is sealed and allows to maintain a high vacuum inside the cryostat.

Two different cooling systems are used in the refrigerator. The first is two stage PulsTube from Cryomech Inc. (PT410), which is capable of cooling the cryostat to a temperature of 4 K. The second is a circulation system of a mixture of He3/He4 isotopes, with which a temperature of 10 mK can be achieved. The PulsTube provides the initial cooling for the condensation of the mixture, which is necessary for the circulation cycle operation.

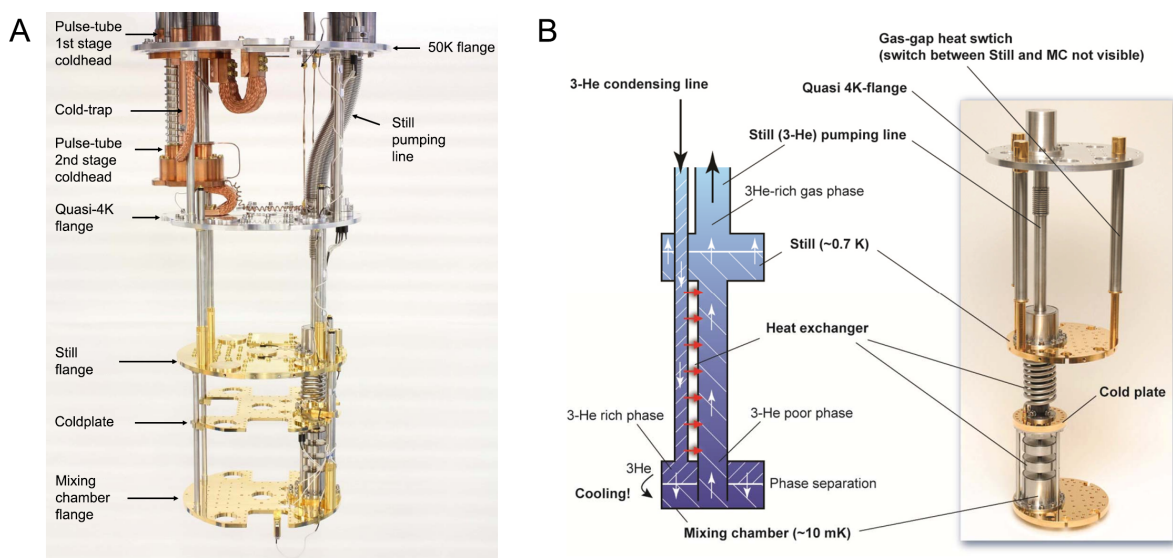


Figure 10: Schemes of the internal arrangement of the dilution refrigerator. Picture A is a real view of the construction of the BlueFors 250LD refrigerator flanges. Picture B shows the arrangement of the helium line and the mixing chamber

Different stages of the cooling process are performed on different plates, so the plates have different base temperature and cooling power. The upper flange closes the cryostat from above, so it is at room temperature. The 50K plate follows, then the Quasi-4K, they are cooled by the first and second PulsTube stages, respectively. Below are Still

plate with $T = 1$ K, Cold plate with $T = 100$ mK and the lowest Mixing Chamber (MC) with $T = 10$ mK. From the uppermost plate to the lowest one there is a pipeline for the circulation of the He3/He4 mixture. On the lowest plate there is a mixing chamber, where the mixture is cooled to the lowest temperature of 10 mK.

The refrigerator requires a number of special supporting equipment, such as compressors, pre-vacuum and turbomolecular pumps, nitrogen traps for helium pipeline, pneumatic system for automatic valve switching.

4.1.2 Operating principle

PulseTube. The operation of the PulseTube cooler is based on the Stirling cycle [14]. The working gas is usually He4 or He3. The feature of this refrigerator is that there are no moving parts in its design (excepting of the compressor, which can be installed away from the cooled body), which reduces thermal friction losses and increases the wear resistance of the product. It is important to note that PulseTube is a closed system, this means that expensive helium does not leak and it does not need to be constantly replenished. A qualitative scheme of the PulseTube is shown in Fig. 11. The sections X_1 and X_3 are thermal tanks with a high temperature T_H (usually room temperature), X_L is a cooled tank with a low temperature T_L . Between the tanks X_1 and X_L there is a regenerative heat exchanger, or simply a regenerator. In this system, the compressor cyclically turns on and off. The gas is compressed by the compressor at a temperature of T_H , then the gas flows through a regenerator, which cools it to a temperature of T_L . Getting into the tube, the gas pushes the gas already in the tube further into the reservoir, compressing it, because of this heat is released on the reservoir. Then the compressor turns off, and the gas begins to return, expanding. It is at this moment that the X_L tank is cooled. From the reservoir, gas flows through a narrow orifice O_1 , which regulates the expansion rate to give the optimum performance. Returning back, the gas passes through the regenerator and is heated to a temperature of T_H , then the cycle repeats.

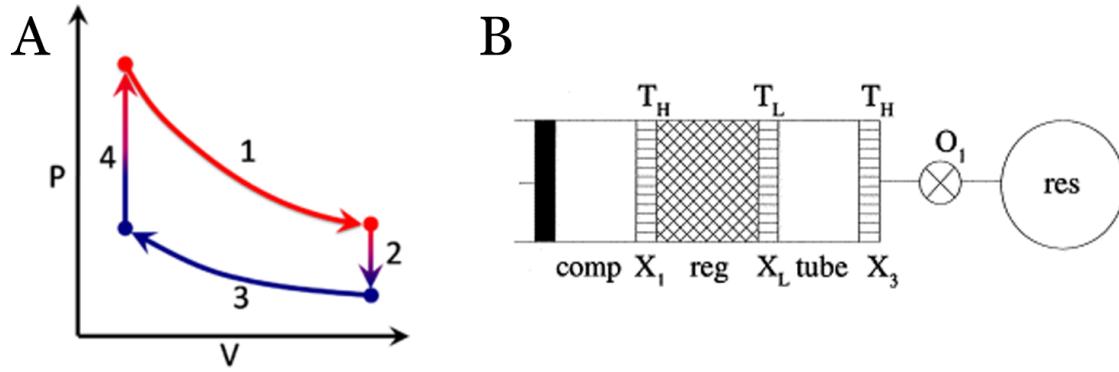


Figure 11: A) A pressure-volume diagram of the idealized Stirling cycle, which includes two isothermal and two isochoric processes. B) Scheme of the internal PulseTube arrangement [14]

He3/He4 circulation. Cooling to 10 mK is based on the characteristics of the He3/He4 isotope mixture [15]. Below 0.8 K in the phase diagram (see Fig. 12) there is an area in which the mixture cannot exist as a whole and it is divided into two phases: with a high concentration of He3 (rich phase) and with a lower (poor phase). In the refrigerator, the mixing chamber is located on the lowest plate, in which the boundary between the phases is located (Fig. 10 B). Since the poor phase is heavier than the rich one, it fills the lower part of the mixing chamber under the influence of gravity above the outlet of the pipe for pumping. Thus, the rich phase is separated from the pumping circuit by the poor phase. Due to the fact that the pressure of saturated He3 vapors is much higher than the pressure of He4 vapors, it is He3 that is mainly pumped out of the poor phase during pumping (even though its concentration in this phase is small). Thus, there is a lack of He3 in the poor phase and due to osmotic pressure, He3 atoms are transferred to the poor phase from the rich one. And here we come to the main point: since the enthalpy of He3 in the poor phase is higher than in the rich one, it is necessary to expend energy to transfer the He3 atom. This energy is taken from the environment and thus cooling occurs up to 10 mK.

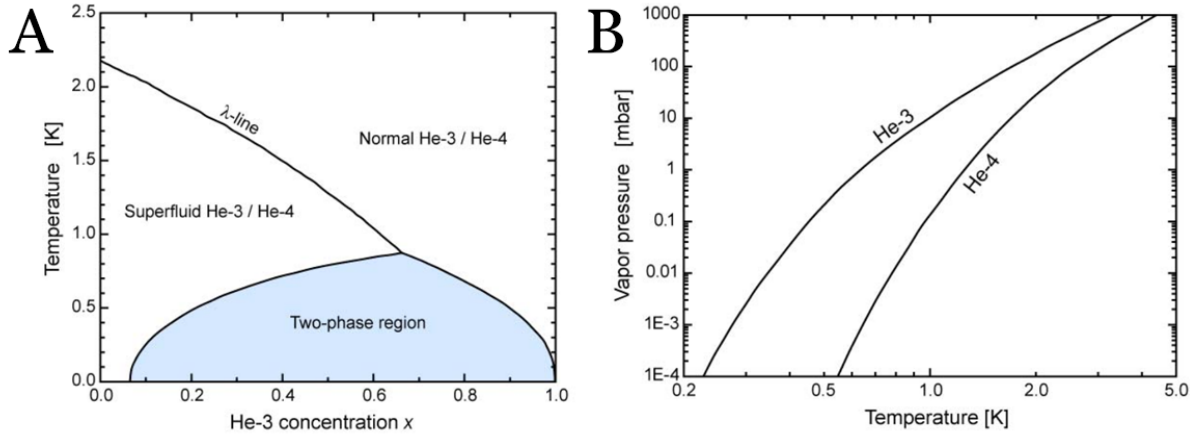


Figure 12: A) The phase diagram of the He3/He4 mixture. B) The dependence of saturated vapor pressure on temperature for He3 and He4

In order to bring the dilution refrigerator to operating mode, a number of preliminary actions are necessary. First, the cryostat is pre-cooled by an auxiliary system, in our case PulseTube, to a temperature of about 4 K. Then, with the help of a compressor, a mixture is fed into the helium circuit at a pressure of about 2 bar. Between the Quasi-4K and Still plates, the mixture flows through flow impedance, so further cooling and condensation of the mixture occurs due to the Joule-Thomson effect. After condensation of a sufficient amount of the mixture, the pumps are switched on and the cooling continues passing the separation temperature of the mixture due to intensive evaporation. After separation of the mixture, the cryostat enters the operating mode and the lowest plate is cooled to a temperature of 10 mK due to the process of moving He3 atoms across the rich and poor phase boundary.

4.2 Sample holder

During this work, a sample holder was designed and created for simultaneous direct current (DC) and radio frequency (RF) measurements. The holder size is $60 \times 38 \times 5$ mm. The holder consists of a base, a top lid, a printed circuit board (PCB) with one DC connector and two SMA connectors.

Metallic shell. Parasitic modes avoiding. The base and lid of the holder are made of oxygen-free copper. Their shape was determined by the shape of the external holder directly attached to the cryostat. An important feature that must be taken into account when designing a closed holder for microwave measurements is the consideration of par-

asitic modes [16]. The fact is that at frequencies above 1 GHz, the wavelength of the radiation becomes the same order as a holder size and any cavity inside it can be considered as a resonator with a set of resonant frequencies, which are called parasitic modes. When the frequency of such a mode is reached, the holder can cause reflection and absorption of the transmitted signal. In order to avoid distortion of the transmitted signal, it is necessary to reduce the size of the cavities in the holder to a size at which all parasitic modes will be above the frequency region of interest. On the other hand, the presence of metal too close to the waveguide will cause a change in its characteristics, which is undesirable. To avoid such effects, it is sufficient that the distance from the waveguide to the walls of the holder is greater than the dimensions of the waveguide. Both of these points were taken into account when designing the holder. Both in the lid and in the base of the holder, cutouts were made along the waveguide. The largest cavity, the size of which cannot be reduced in principle, is the space above the chip area, which has a square section with a side of 14 mm. In such a cavity, resonances begin at a frequency above 15 GHz, which is acceptable for the planned experiments.

Printed circuit board. The printed circuit board is made on the basis of a special dielectric for the microwave range AD1000 with $\varepsilon = 10.2$ and thickness of about 0.5 mm. In order to reduce the reflections of the transmitted signal through the waveguide, it must be matched by an external measuring system, that is, the impedance of the waveguide must be equal to the impedance of the connectors $Z_{out} = 50 \Omega$. Thus, the parameters of the waveguide were chosen so that $Z_{WG} = 50 \Omega$. Parasitic modes can also occur inside the PCB. Moreover, due to the high dielectric constant of the material, their frequencies will be lower than in air. In order to reduce the free cavities inside the board, many metallized holes (via-holes) are made at a distance of about several millimeters.

4.3 Bonding

The pads on the PCB are connected to the contacts on the chip using ultrasonic micro-welding. In this work, the setup from Kulicke & Soffa Industries (Model 4526) was used. A thin aluminum thread with a diameter of about 20 microns is pressed against the target material with a small anvil and welded using ultrasound.



Figure 13: Ultrasonic micro-welding setup (left); a needle with aluminum thread for bonds (top right); a chip in the sample holder connected to the pads by bonds

4.4 Experimental setup

The refrigerator, wires, radio frequency and DC elements and devices, measuring instruments and controllers make up the experimental setup. The sample holder is installed on the lower flange of the refrigerator (see Fig. 14).

Direct current equipment. A line with 8 wires arranged in twisted pairs is conducted from the outside through the refrigerator to the sample holder. In the room, the line is connected to the junction box to which the measuring devices are connected. In this work, Keithley 6221 current source and Keithley 2182A nanovoltmeter were used. A two-stage lowpass RC filter is installed on the Still flange of the refrigerator.

Radio frequency equipment. In this work, the Keysight PNA-L N5232A vector network analyzer (VNA) operating in the range of 300 kHz – 20 GHz was used to measure the transmission coefficient S_{21} . Two coaxial RF cables are conducted from the device to the sample holder. On the input line in the cryostat, attenuators are installed on each flange to reduce thermal noise. On the output line only 0 dB attenuators are installed to improve thermalization of the wires. In addition, the output wires from the MC to 4K flange are made of a superconducting material to reduce signal loss. Between the 4K and 50K flanges, cryogenic amplifier NF-LN 4.16B is installed on the output line, which amplifies the signal in the range from 4 to 16 GHz by 40 dB.

Solenoid. In this work, a superconducting solenoid was used, intended for fields up to 9 T with an inductance of 20 H and a current-to-field ratio: $1 \text{ mA} = 1.068 \cdot 10^{-4} \text{ T}$. The magnet is attached to the 4K flange. A switch heater is installed on this flange, which is a superconducting connection between the magnet wires, which can be switched to normal state using a heater. With this element, it is possible to freeze the magnetic field in the solenoid if the switch heater is in the superconducting state. In all the experiments in this work, the switch heater has always been in a normal state. Its resistance in the normal state at low temperatures is about 20Ω . A YOKOGAWA GS200 DC and voltage source was used as a current source to power the magnet. The source allows to adjust the current in a range of up to 100 mA in step of $1 \mu\text{A}$ and an error = $(0.03\% + 5 \mu\text{A})$.

Temperature control. For temperature control, a thermometer and heater from the refrigerator were used, which are located on the lower flange (MC). A PID controller is used to maintain a constant temperature during measurements.

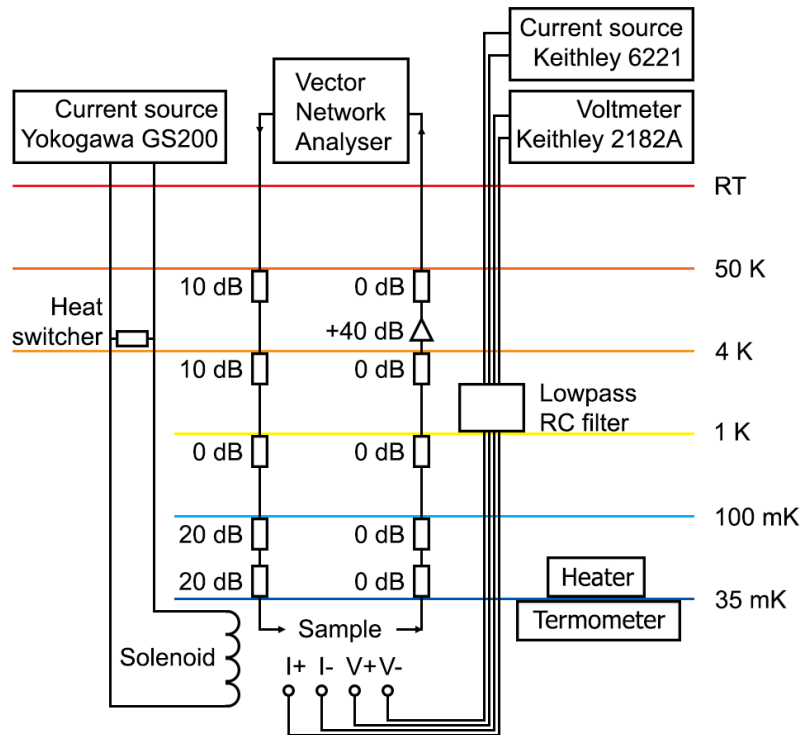


Figure 14: A scheme of the experimental setup, that demonstrates the arrangement of wires, DC and RF elements inside the refrigerator and the used measuring equipment

5 Samples

5.1 Design

The sample consists of a central measuring coplanar waveguide (with RF input and output ports), six resonators, four structures for DC measurements and crosses for alignment layers during lithography. The design of the sample is shown in Fig. 15.

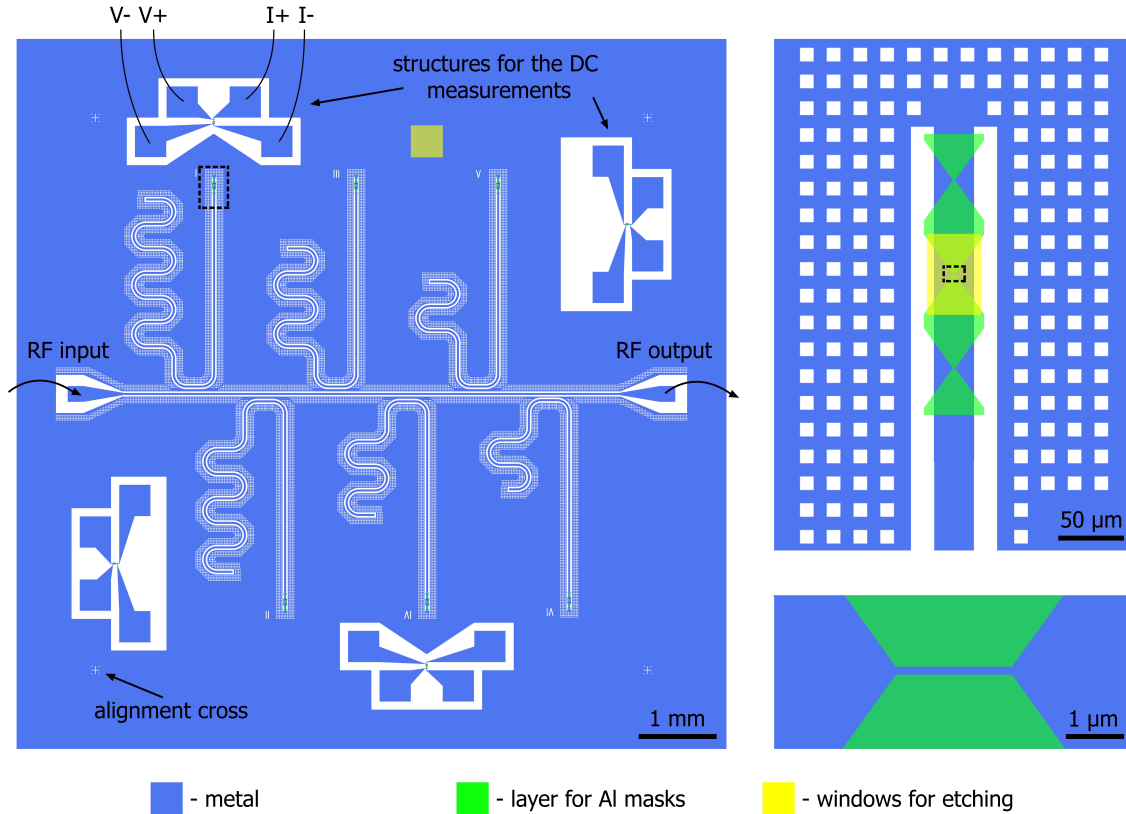


Figure 15: Left: image of the samples design using in this work. There is a measuring waveguide in the center, with which six $\lambda/4$ resonators are capacitively connected, four structures with contacts for DC measurements using the four-terminal Kelvin method are located on the sides of the chip. Top right: the enlarged image of a part of the resonator with windows for lithography of SNS transitions. Bottom right: enlarged image of a window for the lithography of the gap for Josephson SNS junction.

The resonator frequencies are designed in the range 3.5 – 6 GHz. The ratio of the center line width and the gap was chosen so that the impedance of the line was 50Ω : $W = 30 \mu\text{m}$, $G = 17 \mu\text{m}$. Around the resonators and waveguide there are rows of square holes with a size of 10×10 microns, which play the role of magnetic flux traps. On the central

line of the resonators and central part of DC structures sandglass-like windows with a thin gap are made for aluminum masks sputtering. These structures are duplicated (on resonators three times, on DC structures twice) to increase the percentage of successful results. After sputtering aluminum, the sample was viewed on SEM and one, the most successful structure was selected. Then the sample was covered with a protective layer of the resist and the etching windows were lithographed only for the selected structures. In addition, a large window was lithographed in niobium film for the ellipsometer beam in the etching setup.

5.2 Fabrication process

The samples were made on high-resistance silicon substrates from the company Silicon Materials with orientation $\langle 100 \rangle$ and $\rho > 10^4 \Omega \cdot \text{cm}$. Firstly, two wafers 10 mm were cleaned in IPA and acetone. Then bilayer of copper (bottom layer) and niobium (top layer) was sputtered on the both substrates simultaneously using the magnetron sputtering method in Institute of Solid State Physics RAS. The whole process of fabricating structures can be divided into two main stages: the creation of micrometer objects and the creation of nanoobjects. Both samples passed the first stage at the Laboratory of Superconducting Metamaterials in MISIS. The first stage includes laser lithography, then plasma chemical etching of the top layer (niobium) and, finally, wet etching of the bottom layer (copper). Thus, as a result of this process, both metals were removed in the gaps up to silicon. After the first stage, the Sample #1 was sent for measurements, and the Sample #2 for further fabrication.

The second stage begins with creating a mask for etching the niobium layer to create Josephson SNS junctions. The mask consists of two layers. The bottom layer is made of aluminum with a thickness of 20 nm for precise etching of the Josephson junctions gap. The use of aluminum masks has a number of advantages over an electron resist. Firstly, oxygen in the composition of gases for plasma chemical etching of niobium etches the resists, therefore, an undesirable widening of the gap is inevitable due to horizontal etching of the resist. In addition, in order for the resist to survive the etching of 100 nm of niobium, its thickness of about 200 nm is necessary, which reduces the resolution of E-beam lithography. Aluminum is not etched by plasma chemistry, so it is possible to create masks up to 20 μm thick. Due to the presence of a significant height difference in the sample (150 nm), an additional protective layer of the mask is required except aluminum. The second layer of the mask was made of a electronic resist with windows for etching. After niobium etching, Sample #2 was analyzed using Scanning Electron Microscope (see

next section). Before the measurements, the aluminum masks were removed.

After the measurements, it was decided to make changes to Sample #2. Namely, to remove the copper sections remaining after niobium etching near the SNS junctions. This was done using E-beam lithography and physical plasma etching.

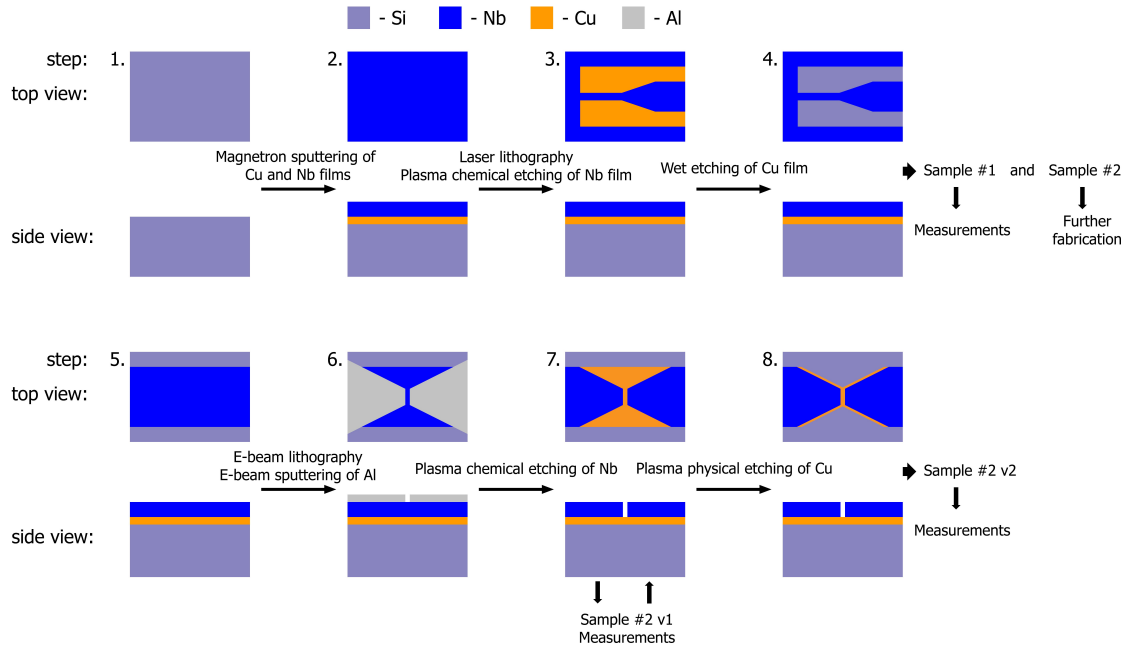


Figure 16: The scheme of the sample fabrication process used in this work.

5.3 SEM

The Sample #2 was analyzed using a Scanning Electron Microscope (SEM). Using the obtained images shown in Fig. 17, the main dimensions of the fabricated structures were measured (see Table 9).

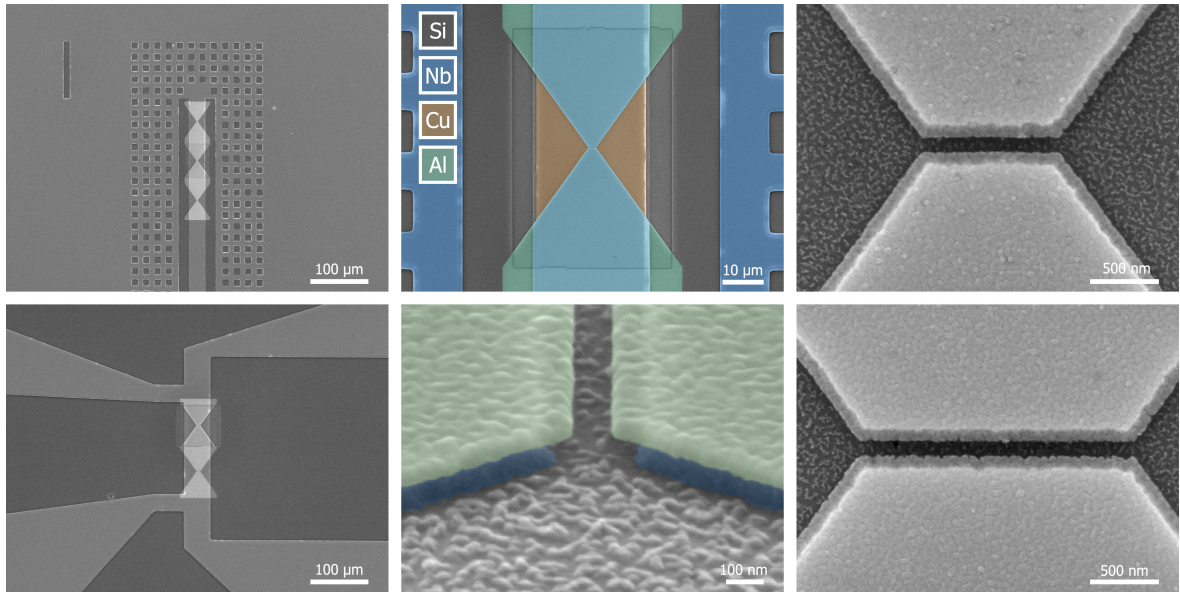


Figure 17: Pictures of the fabricated sample obtained using SEM

Table 9: The main dimensions of the fabricated structures

Resonator central line width	28.4 μm
Resonator gap width	17.0 μm
Width of the “Narrow” SNS	930 nm
Width of the “Wide” SNS	1870 nm
Length of SNS	280 nm

6 Results and Discussion

6.1 Resonators spectroscopy

This section we will describe the measurements of resonators on a niobium/copper bilayer without SNS (Sample #1). In the experiment, the complex transmission coefficient S_{21} is measured depending on the frequency of the signal. Resonance appears as a drop in the amplitude of the signal at a certain frequency. During measuring of Sample #1, no external amplifiers were used, and the additional attenuation without wires was 20 dB.

6.1.1 Resonators parameters

To determine the parameters of a resonator, the approximation according to the expression (ref) is used. Fitting is performed by the program from the article [17]. Figure 18 shows an example of the measured resonant peak of Resonator #1 and its fit. As can be seen, fit describes the experimental data with high accuracy, taking into account the asymmetry of the peak. The measurements were carried out at the refrigerator base temperature $T = 16$ mK.

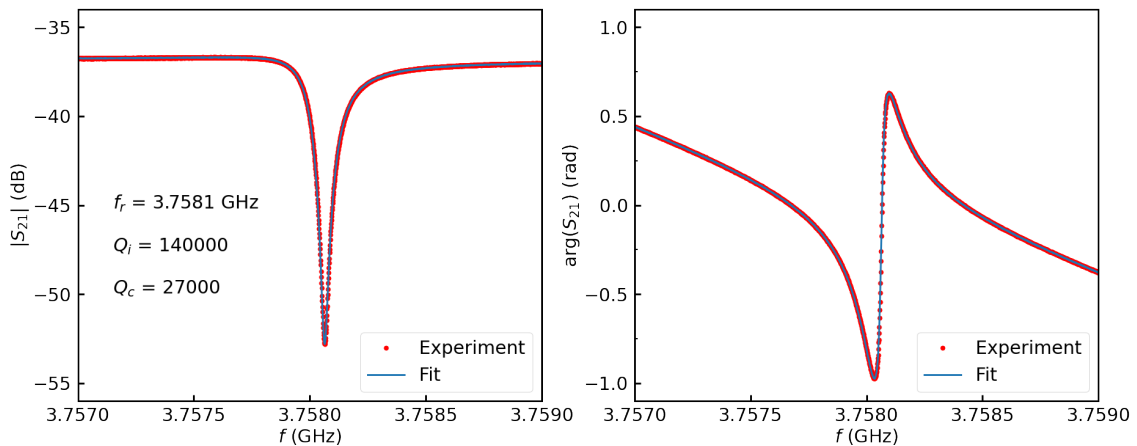


Figure 18: Experimental data and fit of the dependence of the amplitude (left) and phase (right) of the transmission parameter S_{21} on the frequency

There are a number of theoretical formulas that allow us to determine some characteristics of the resonator even before the experiment. The resonant frequency can be determined from the resonator geometric dimensions and the dielectric constant of the substrate according to the formula (ref). For calculations, the permittivity of silicon at low temperatures $\varepsilon = 11.45$ was taken [18]. Formulas for determining the coupling Q-factor are

presented in [19]. An example of a theoretical preliminary calculation and the results of experimental measurements of resonator parameters are presented in the Table 10.

Table 10: Results of theoretical calculations and measurements of resonator characteristics

Parameter	Theoretical value	Experimental value	Error
f_r , GHz	3.78	3.758065	$5 \cdot 10^{-6}$
Q_c	48000	27000	300
Q_i		140000	1500
Q_l		22600	400
$\Delta f_{1/2}$, MHz		0.167	0.002
ϕ , rad		0.23	0.02

6.1.2 Temperature dependence

The resonators parameters were measured depending on the temperature in the range from 16 mK to 9 K. The change in the parameters at low temperatures is mainly due to the temperature dependence of the surface impedance of the superconducting film[20, 21]. There are several models with different degrees of accuracy to describe this dependence [22]. However, there is an additional layer of copper in our sample, which is not taken into account in the exact theories, so their use is unreasonable. A qualitative explanation of the resonator frequency dependence on temperature is that the kinetic inductance of a superconductor in thin films depends on the concentration of Cooper pairs $L_K \propto n_s^{-1}(T)$, which qualitatively depends on temperature as $n_s(T) \propto [1 - (T/T_c)^4]$ (the Gorter-Casimir dependence). Fig. 19 shows the measured parameters for the first and second harmonics of the Resonator #1 and the first harmonic of the Resonator #3. The data are normalized to values at a base temperature of 16 mK. The universality of the relative frequency dependence is explained by the fact that the ratio of the linear kinetic inductance to the geometric one does not depend on a resonator.

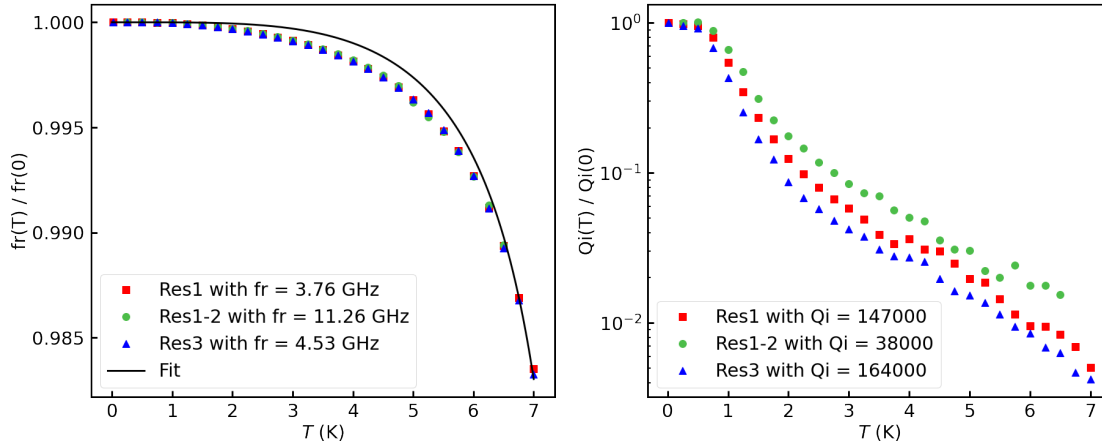


Figure 19: Measured resonance frequency (left) and internal quality factor(right) for the first and second harmonics of the Resonator #1 and the first harmonic of the Resonator #3. The data are normalized to values at a base temperature.

6.2 Direct current measurements of SNS junctions

To characterize the fabricated Josephson junctions, direct current measurements of special structures along the edges of the chip were carried out (see section Sample: Design). Current–voltage characteristics were measured depending on temperature and external magnetic field using the four-terminal Kelvin method. Two structures with different widths of SNS junctions: “Narrow” and “Wide” types were measured (see section Sample: SEM).

6.2.1 Current–voltage characteristics

At the base temperature $T = 35$ mK, the dependence of the voltage at the Josephson junctions on the current flowing through them was measured. The measurement results are shown in Fig. 20. The obtained current–voltage curves differ from the theoretical dependence (see section 2.2.2) by a sharp jump in voltage when the critical current is reached and the presence of hysteresis. This difference is explained by the overheating of the SNS junction [23], which is expected in our samples due to the large value of the critical current.

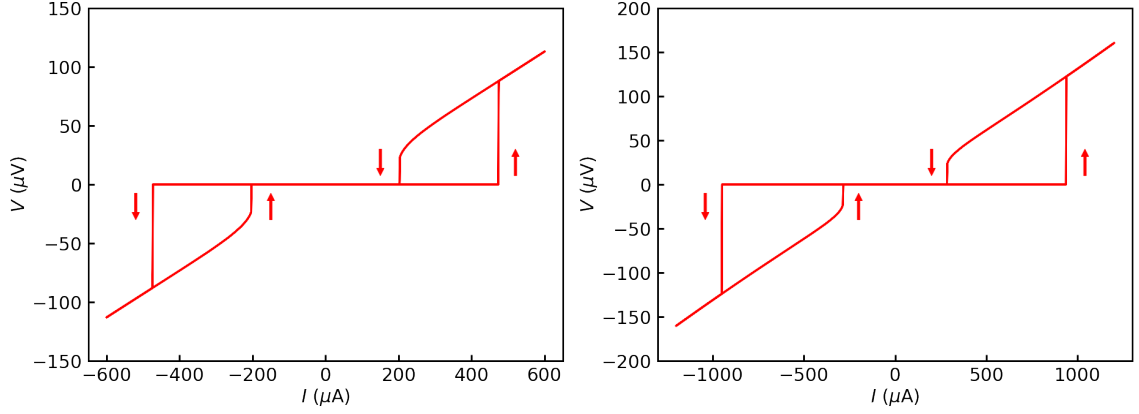


Figure 20: Measured current–voltage characteristics of “Narrow” type (left) and “Wide” type (right) SNS junctions

Based on the measured current–voltage characteristics, the main parameters of the two types of SNS used in this work (“Narrow” and “Wide”) were obtained. Here and further, the critical current during measurements with decreasing current is denoted as I_b . The measurement results are shown in the table 11. As can be seen from the resulting values of λ_J , both “Narrow” and “Wide” junctions cannot be considered as short, since their width is greater than λ_J , and the magnetic field in them is not uniform. On the other hand, the width of the “Narrow” contact is slightly less than the minimum required for the existence of a free Josephson vortex in $4\lambda_J$, and the “Wide” transition is larger.

Table 11: Main characteristics of Josephson junctions

Sample	“Narrow”	“Wide”
W	930 nm	1870 nm
I_c	473 μA	942 μA
I_b	202 μA	284 μA
j_c	1.0×10^{10} A/m ²	1.0×10^{10} A/m ²
R_N	200 m Ω	147 m Ω
V_c	95 μV	140 μV
λ_J	245 nm	245 nm
W/ λ_J	3.8	7.6

6.2.2 Dependence on the magnetic field

At the base temperature $T = 35$ mK, the current-voltage characteristics of the Josephson junctions were measured depending on the external magnetic field. Then, using the cut-off method at the voltage $V_{\text{threshold}} = 200$ nV, the maximum superconducting current through the junction I_{max} was determined. In the simplest case, when the field inside the transition can be considered homogeneous, the dependence of I_{max} on the external magnetic field is described by the Fraunhofer dependence (19). However, in our case, both types of junctions are wide enough for the field to be non-uniform. At the same time, as assumed by the theory, the value of the normal resistance R_N does not depend on the magnetic field. The measurement results are shown in Fig. 21. Sharp jumps are not repeatable and are most likely associated with the movement of Abrikosov vortices. The fact is that due to the high pinning and low temperature, the configuration of the Abrikosov vortices is not in an equilibrium state and creates an additional local field through the SNS junction.

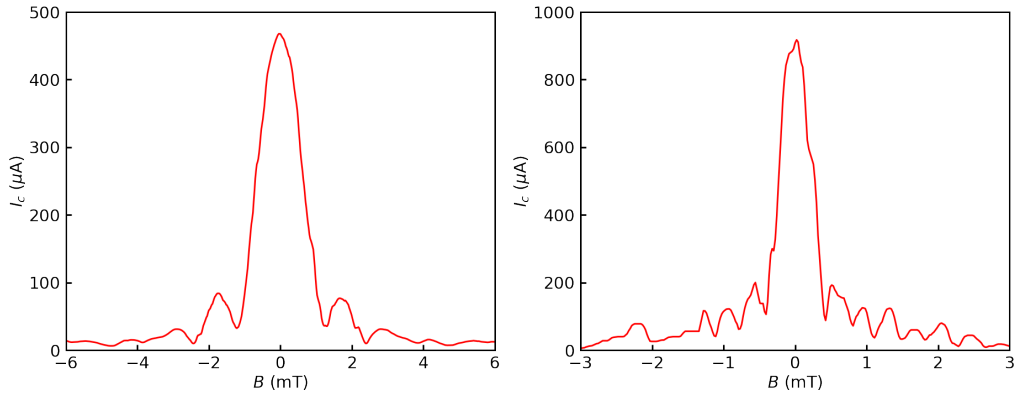


Figure 21: Measured dependence of the maximum superconducting current through the “Narrow” type (left) and “Wide” type (right) SNS junctions on the magnetic field

6.2.3 Dependence on the temperature

The current-voltage curves of the junctions were measured as a function of temperature. Then, using the cut-off method at the voltage $V_{\text{threshold}} = 100$ nV, the critical current I_c and the return current due to overheating of SNS I_b were determined. Results of the dependence of I_c and I_b on temperature are shown in Fig. 22. The return current I_b weakly depends on temperature. The hysteresis of the current-voltage curve disappears at temperature 1.1 K for “Narrow” junction and at 1.5 K for “Wide” one. The value of the normal resistance R_N does not depend on the temperature within the measurement error. In general, the theory for describing the temperature dependence of the Josephson

junction critical current is complex and depends on the materials and geometry of the contact [24]. In our case, SNS correspond to the type of long junctions, where the influence of interfaces can be neglected and the theoretical dependence is simplified [25].

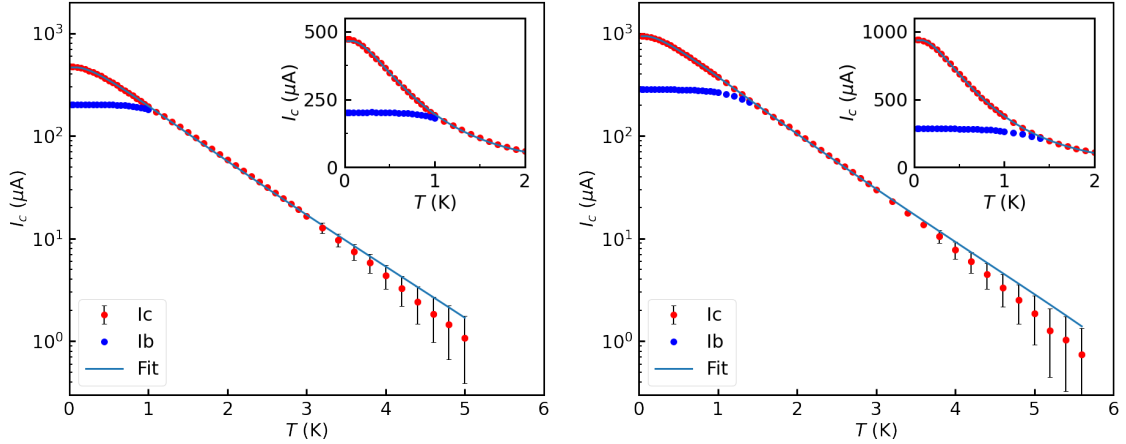


Figure 22: Dependence of the critical and return current on temperature for “Narrow” (left) and “Wide” (right) types of SNS junctions

6.3 Spectroscopy of resonators with SNS

This section we will describe the measurements of resonators on a niobium/copper bilayer with Josephson SNS junction (Sample #2).

6.3.1 Resonances overview

Standard measurements of the transmission coefficient S_{21} dependence on the signal frequency were carried out. The resonators on the Sample #2 were supplemented with SNS junctions compared to the Sample #1 (see section 5.2). During the measurements, it turned out that the internal Q-factor of the resonators with SNS became orders of magnitude smaller (see Fig. 23). Such a strong decrease in Q-factor is due to the fact that after niobium etching for creation SNS junctions, there were areas with open copper on the central line of the resonator, which is no longer proximized by the niobium layer as on the rest of the sample. Thus, open copper creates additional dissipation. The change in the resonance frequency is mainly due to a change in the geometry of the resonator section, which locally changed the linear inductance and capacitance.

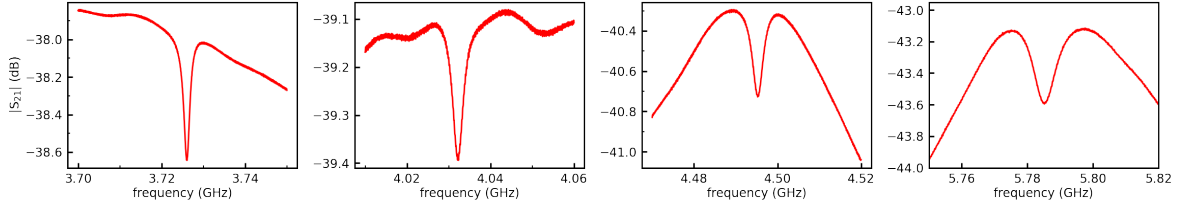


Figure 23: Measured dependencies of the transmission coefficient amplitude on the frequency for four resonators of Sample #2

6.3.2 RF scan in the magnetic field. Josephson and Abrikosov vortexes detection

Resonant responses were measured in the $S_{21}(f)$ parameter depending on the external magnetic field at the base temperature $T = 35$ mK. The experiment was carried out in order to detect Josephson vortexes in the SNS junction inserted into the resonator. However, it should be noted that the resonator can also be affected by Abrikosov vortexes that penetrate the superconducting film. Thus, one of the objectives of this experiment was to identify differences in the influence on the resonator of two types of vortexes.

In the experiment, two resonators #1 and #2 with different widths of SNS junctions were measured: “Wide” and “Narrow” type respectively. Recall that the width of the “Wide” SNS junction is sufficient for the existence of a free Josephson vortex in it, and the “Narrow” transition is slightly shorter for this (see section 6.2.1). The magnetic field was applied for the first time after the sample was heated above T_c . Fig. 24 shows the measurement results.

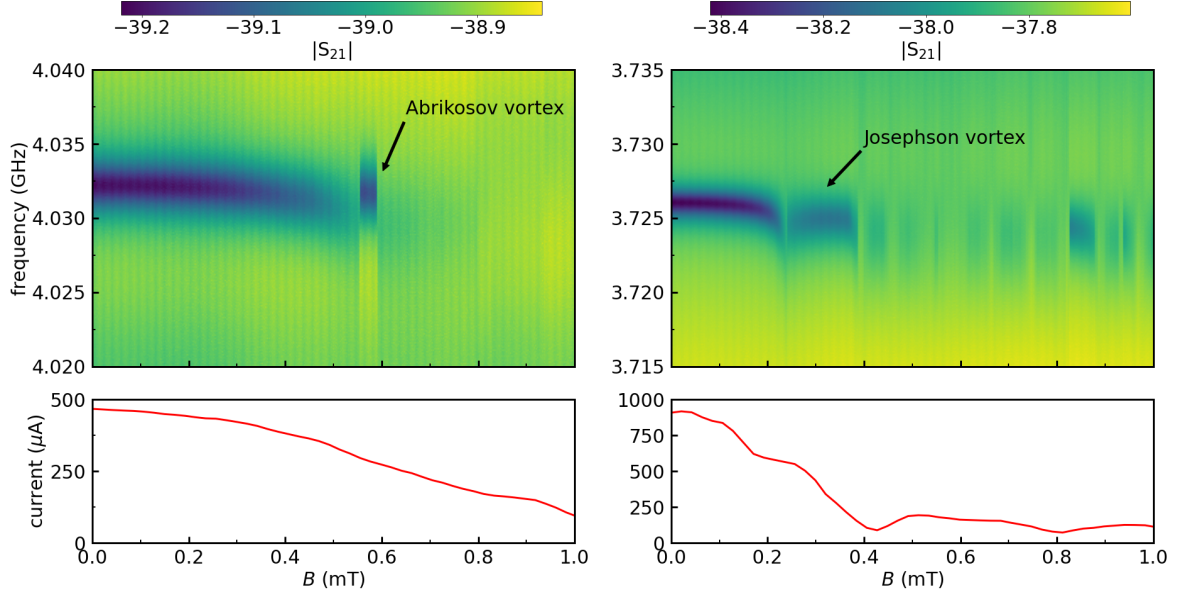


Figure 24: Top row – scans of the transmission parameter in the magnetic field for the resonator with “Narrow” (left) and “Wide” (right) type of SNS junction. Bottom row – the maximum supercurrent dependence on the magnetic field for the corresponding SNS junctions

First consider a scan of the Resonator #2 with a “Narrow” type of SNS junction. This scan shows a smooth attenuation of the resonance, then an unexpected sharp jump in frequency and Q-factor, and further the absence of a signal. Most likely, the sharp jump is associated with the Abrikosov vortex (vortexes), since the width of the SNS transition is too small for the entry of the Josephson vortex. When the Abrikosov vortex (vortexes) overcomes the surface barrier and penetrates the film, it abruptly changes the local magnetic field through the SNS junction. The subsequent sudden disappearance of the resonance may be due to the fact that the vortex (vortexes) broke away from the pinning centers and moved deep into the film away from the junction.

There is a qualitatively different picture on the scan of Resonator #1 in small fields. The resonance at first also smoothly shifts and attenuates, but then it is recover to a some value. At that moment, the resonator switched to a different state. Since this state differs from the entry of the Abrikosov vortex (as in the scan of Resonator #2) and since the width of the SNS junction of Resonator #1 is sufficient for the existence of a free Josephson vortex in it, we conclude that in the fields from 2.4 mT to 3.8 mT the resonator is in a state with one Josephson vortex in the SNS junction. In large fields, Resonator #1 is also affected by Abrikosov vortexes. The following is a list of experimentally revealed differences in the effect of Josephson and Abrikosov vortexes on the resonator:

- Before entering/exiting of the Josephson vortex the resonance smoothly shifts and attenuates, while the entering/exiting of the Abrikosov vortex occurs in less than one step of the field sweep
- States with Josephson vortices are stable and precisely repeatable (see the next section), while states with Abrikosov vortices are not repeatable
- Josephson vortices begin to penetrate in smaller fields than Abrikosov ones, since both vortices carry a quantum of magnetic flux, but the dimensions of Josephson vortex is larger ($\lambda_J > \lambda_L$)

6.3.3 Analysis of Josephson vortices

In the measurements of the Resonator #3 with SNS junction of the “Wide” type, it turned out to detect up to of 3 Josephson vortices (see Fig. 25).

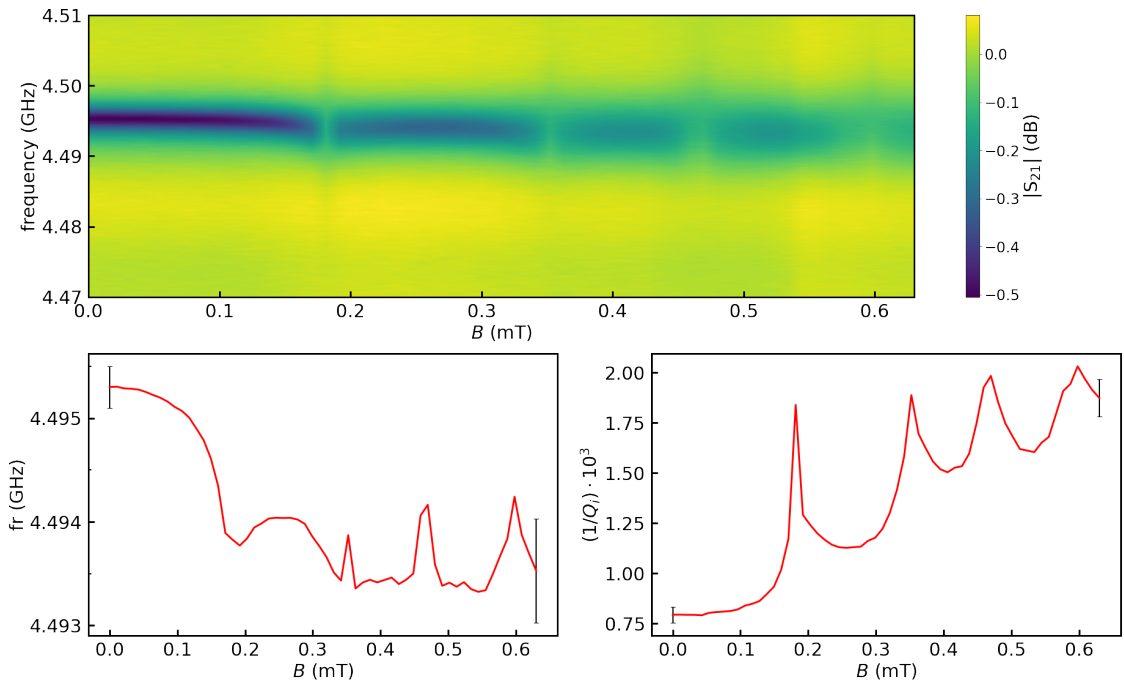


Figure 25: A scan of the transmission parameter in the magnetic field for the Resonator #3 with “Wide” type of SNS junction (top). Dependence of resonance frequency (bottom left) and inverted internal quality factor (bottom right) on the magnetic field

The effect of the vortices can be described quantitatively by changing the parameters of the resonator, and then it is possible to determine the impedance of the SNS junction with vortices in it. Due to the decrease in Q-factor, the resonant frequency is determined with

a large error and cannot be analyzed. But it is possible to investigate the dependence of internal Q-factor. Figure 25 shows the results of the experiment, the dependence of $1/Q_i$ on the magnetic field is directly related to the real part of the impedance of the SNS junction (53) and is qualitatively consistent with the theory [26].

6.3.4 Edge barrier effect

The states with Josephson vortices are repeatable, however, when the direction of the field sweep is changed, hysteresis is observed in the scans (see Fig. 26). So, vortices exit the SNS junction in fields smaller than the entry field. In addition, the scan is not symmetrical with respect to the magnetic field: before the entrance/exit of the vortex, the resonance smoothly shifts and decreases, and after the entrance/exit almost does not change. This behavior is evidence of the presence of an edge barrier for Josephson vortices, similar to the Bean-Livingstone surface barrier for Abrikosov vortices.

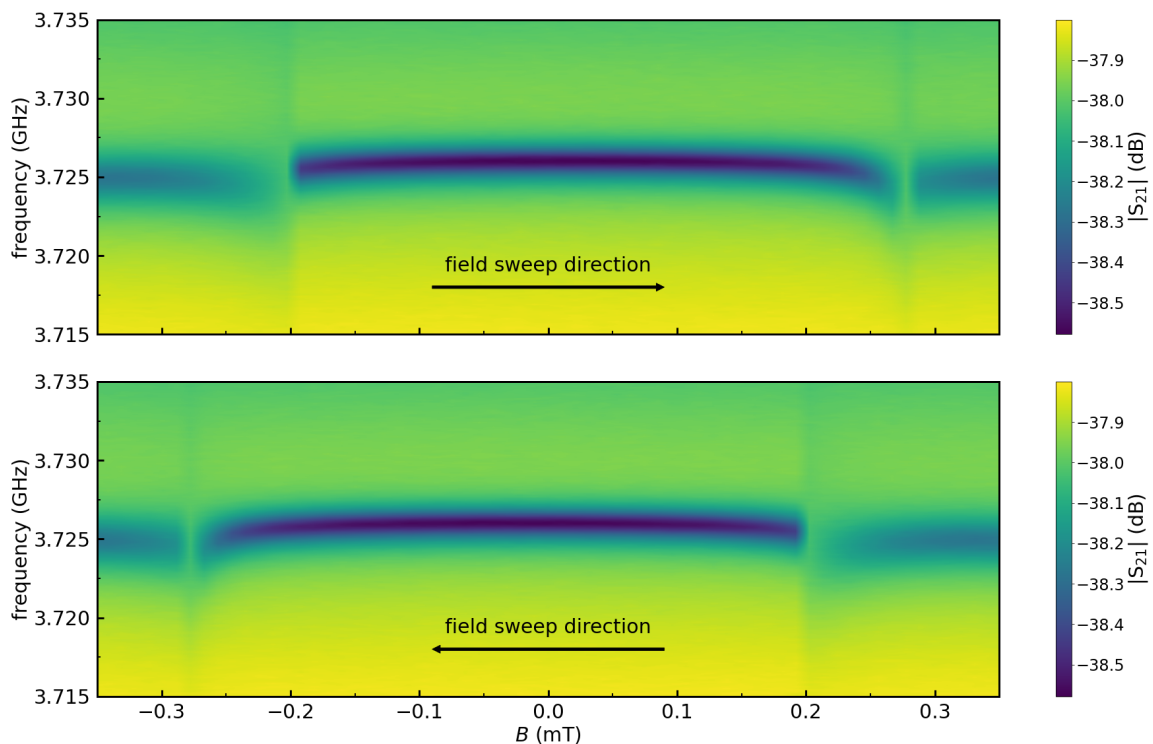


Figure 26: A scan of the transmission parameter in the magnetic field for the Resonator #1 with “Wide” type of SNS junction with different field sweep directions.

6.3.5 Switching states

Using the hysteresis in states with different numbers of vortices, an experiment with switching between them was conducted. The sample was fed a signal at a fixed frequency $f_0 = 3.7252$ GHz and power $P = -20$ dBm. The frequency was chosen to be equal to the resonant frequency of Resonator #1. Thus, the amplitude of the output signal depends on the state of the resonator. A constant magnetic field $B = 0.192$ mT was applied to the sample. The states were switched by current pulses through the solenoid. An example of switching is shown in Fig. 27. It should be noting that a switch heater is connected in parallel to a superconducting solenoid (see section 4.4). So this system works as a lowpass filter and the current through the solenoid does not change instantly, but relaxes to a given value with a characteristic time $\tau = \sqrt{L/R} \sim 1$ s. Thus the duration of the current pulses in the experiment was 1 s and the states were switched in a time of the order of τ .

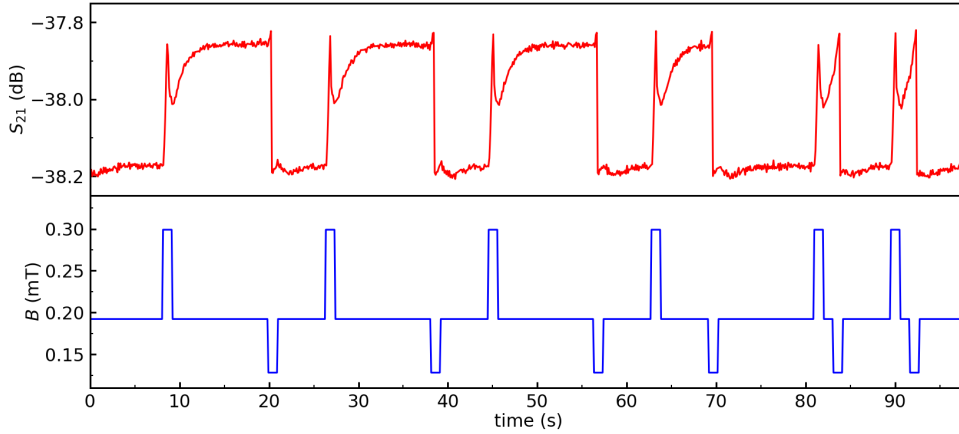


Figure 27: Experiment on switching the resonator state in real time. The top picture shows the change in the transmission coefficient at a constant frequency and power over time. The bottom picture shows the change in the magnetic field through the solenoid.

6.3.6 Nonlinear response

The resonators in Sample #2 had too low Q-factor (and, consequently, the current gain) so that using available equipment, it was impossible to overcome the critical current through the SNS junction in the resonators. After the first measurements with Sample #2, sections of open copper were removed from the center line of the resonators near the SNS (see sections 5.2 and 6.3.1). After that, the Q-factor of the resonators indeed increased. On the modified sample, it was possible to observe nonlinear effects caused by overcoming the critical SNS junction (see Fig. 28)

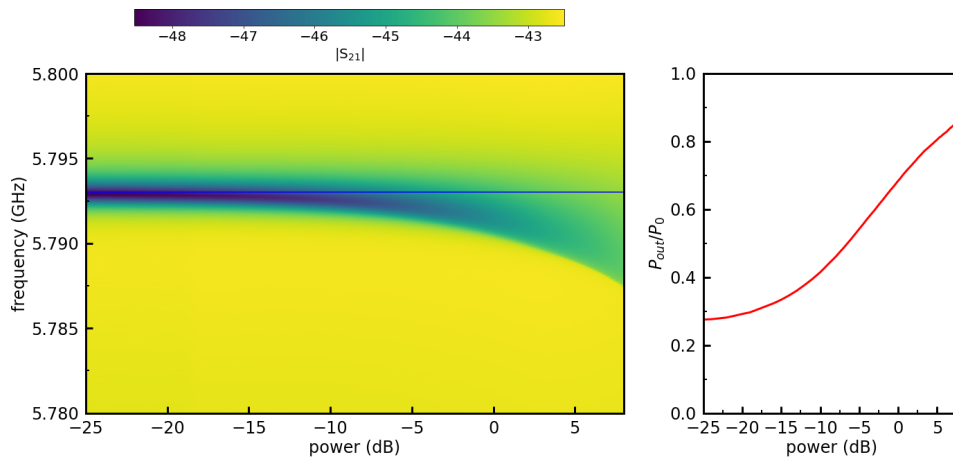


Figure 28: The dependence of the transmission coefficient on the frequency and power of the input signal (left). The right picture shows a slice of the left plot at the frequency marked with a blue line.

7 Conclusion

During this work, several samples of resonators with different types of Josephson SNS junctions were fabricated for the study of Josephson vortices by microwave resonance spectroscopy. During the experiments, the parameters of resonators with SNS junctions were measured depending on the signal power, the external magnetic field and the temperature in the dilution refrigerator.

As one of results of this work, a well-controlled and repeatable process of fabrication of planar resonators on a niobium/copper bilayer with planar Josephson SNS junctions was developed. Using the manufactured samples, a strong dependence of the resonator parameters on the input signal power was demonstrated due to the nonlinear current–voltage characteristic of the Josephson junction. Such a nonlinear microwave element can be used in advanced computing systems, such as neuromorphic computers.

Moreover, the work showed the possibility of detecting the individual Josephson vortices inside the SNS junction in the resonator, providing an opportunity to study their individual and collective behavior using microwave radiation. Experiments have shown that, unlike Abrikosov vortices, states with Josephson vortices are stable and precisely repeatable, and have hysteresis due to the edge barrier effect. The controllability of the system makes it possible to use it in logic circuits. For example, in this paper, the possibility of using Josephson vortices as a memory element in a microwave system was demonstrated.

References

- [1] A. Barone and G. Paternò. *Physics and Applications of the Josephson Effect*. Wiley, 1982.
- [2] Frank Arute, Kunal Arya, Ryan Babbush, and et al. Quantum supremacy using a programmable superconducting processor. *Nature*, 574(7779):505–510, 2019.
- [3] Sergey K Tolpygo, Vladimir Bolkhovsky, Ravi Rastogi, Scott Zarr, Alexandra L Day, Evan Golden, Terence J Weir, Alex Wynn, and Leonard M Johnson. Advanced fabrication processes for superconductor electronics: Current status and new developments. *IEEE Transactions on Applied Superconductivity*, 29(5):1–13, 2019.
- [4] Andrey Schegolev, Nikolay Klenov, Igor Soloviev, and Maxim Tereshonok. Learning cell for superconducting neural networks. *Superconductor Science and Technology*, 34(1):015006, Nov 2020.
- [5] A.V. Ustinov. Solitons in josephson junctions. *Physica D: Nonlinear Phenomena*, 123(1):315–329, 1998. Annual International Conference of the Center for Nonlinear Studies.
- [6] Y. M. Habib, C. J. Lehner, D. E. Oates, L. R. Vale, R. H. Ono, G. Dresselhaus, and M. S. Dresselhaus. Measurements and modeling of the microwave impedance in high- T_c grain-boundary josephson junctions: Fluxon generation and rf josephson-vortex dynamics. *Phys. Rev. B*, 57:13833–13844, Jun 1998.
- [7] V. V. Schmidt. *The Physics of Superconductors*. Springer Berlin, Heidelberg, 1997.
- [8] M. Tinkham. *Introduction to Superconductivity*. Dover Books on Physics Series. Dover Publications, 2004.
- [9] B.D. Josephson. Possible new effects in superconductive tunnelling. *Physics Letters*, 1(7):251–253, 1962.
- [10] R. Gross, A. Marx, and F. Deppe. *Applied Superconductivity: Josephson Effect and Superconducting Electronics*. De Gruyter Textbook Series. Walter De Gruyter Incorporated, 2016.
- [11] D. Pozar. *Microwave Engineering*. Wiley, 4th edition, 2011.
- [12] Marc J. Madou. *Fundamentals of Microfabrication and Nanotechnology*, volume 2. CRC Press, 3th edition, 2011.

- [13] BlueFors Cryogenics. *BF-LD250 User manual*, 1.4.0 edition, 2013.
- [14] A.T.A.M de Waele. Pulse-tube refrigerators: principle, recent developments, and prospects. *Physica B: Condensed Matter*, 280(1):479–482, 2000.
- [15] R. Radebaugh and J.D. Siegwarth. Dilution refrigerator technology. *Cryogenics*, 11(5):368–384, 1971.
- [16] A. S. Averkin, A. Karpov, K. Shulga, E. Glushkov, N. Abramov, U. Huebner, E. Il'ichev, and A. V. Ustinov. Broadband sample holder for microwave spectroscopy of superconducting qubits. *Review of Scientific Instruments*, 85(10):104702, 2014.
- [17] S. Probst, F. B. Song, P. A. Bushev, A. V. Ustinov, and M. Weides. Efficient and robust analysis of complex scattering data under noise in microwave resonators. *Review of Scientific Instruments*, 86(2):024706, 2015.
- [18] Jerzy Krupka, Jonathan Breeze, Anthony Centeno, Neil Alford, Thomas Claussen, and Leif Jensen. Measurements of permittivity, dielectric loss tangent, and resistivity of float-zone silicon at microwave frequencies. *IEEE Transactions on microwave theory and techniques*, 54(11):3995–4001, 2006.
- [19] Ilya Besedin and Alexey P Menushenkov. Quality factor of a transmission line coupled coplanar waveguide resonator. *EPJ Quantum Technology*, 5(1):1–16, 2018.
- [20] Takashi Noguchi, Agnes Dominjon, Matthias Kroug, Satoru Mima, and Chiko Otani. Characteristics of very high q nb superconducting resonators for microwave kinetic inductance detectors. *IEEE Transactions on Applied Superconductivity*, 29(5):1–5, 2019.
- [21] Luigi Frunzio, Andreas Wallraff, David Schuster, Johannes Majer, and Robert Schoelkopf. Fabrication and characterization of superconducting circuit qed devices for quantum computation. *IEEE transactions on applied superconductivity*, 15(2):860–863, 2005.
- [22] JP Turneaure, J Halbritter, and HA Schwettman. The surface impedance of superconductors and normal conductors: The mattis-bardeen theory. *Journal of Superconductivity*, 4(5):341–355, 1991.
- [23] H. Courtois, M. Meschke, J. T. Peltonen, and J. P. Pekola. Origin of hysteresis in a proximity josephson junction. *Phys. Rev. Lett.*, 101:067002, Aug 2008.

- [24] A. A. Golubov, M. Yu. Kupriyanov, and E. Il'Ichev. The current-phase relation in josephson junctions. *Reviews of modern physics*, 76(2):411, 2004.
- [25] P Dubos, H Courtois, B Pannetier, and et al. Josephson critical current in a long mesoscopic sns junction. *Physical Review B*, 63(6):064502, 2001.
- [26] Z. Zhai, Patanjali V. Parimi, and S. Sridhar. Nonlinear microwave impedance of short and long josephson junctions. *Phys. Rev. B*, 59:9573–9580, Apr 1999.